BRNO UNIVERSITY OF TECHNOLOGY

Faculty of Mechanical Engineering

MASTER'S THESIS

Brno, 2023

Bc. David Kugler

BRNO UNIVERSITY OF TECHNOLOGY
VYSOKÉ UČENÍ TECHNICKÉ V BRNĚ

FACULTY OF MECHANICAL ENGINEERING
FAKULTA STROJNÍHO INŽENÝRSTVÍ

INSTITUTE OF PHYSICAL ENGINEERING
ÚSTAV FYZIKÁLNÍHO INŽENÝRSTVÍ

GROWTH OF ORGANIC HETEROSTRUCTURES ON METAL SURFACES

RŮST ORGANICKÝCH HETEROSTRUKTUR NA POVRCHU KOVŮ

MASTER'S THESIS
DIPLOMOVÁ PRÁCE

AUTHOR AUTOR PRÁCE	Bc. David Kugler
SUPERVISOR VEDOUCÍ PRÁCE	Ing. Pavel Procházka, Ph.D.

BRNO 2023

Assignment Master's Thesis

Institut:	Institute of Physical Engineering
Student:	**Bc. David Kugler**
Degree programm:	Physical Engineering and Nanotechnology
Branch:	no specialisation
Supervisor:	**Ing. Pavel Procházka, Ph.D.**
Academic year:	2022/23

As provided for by the Act No. 111/98 Coll. on higher education institutions and the BUT Study and Examination Regulations, the director of the Institute hereby assigns the following topic of Master's Thesis:

Growth of organic heterostructures on metal surfaces

Brief Description:

Organic semiconductors are employed worldwide, and any improvement in their efficiency would lead to significant economic savings in the semiconductor industry with direct environmental implications. In the thesis, the student will study the growth and behavior of well–known organic molecules such as pentacene, helicene, or HATCN deposited on top of a monolayer of carboxylic acid molecules prepared on the surface of a silver crystal under ultra–high vacuum conditions. Low–energy electron microscopy, X–ray photoelectron spectroscopy, and scanning tunneling microscopy will be used for characterization.

Master's Thesis goals:

1) Review the current state of the art in the field of organic semiconductors on metal surfaces.
2) Prepare monolayers of carboxylic acids (BDA, BTB, or their mixed phases with pentacene) on the monocrystalline silver substrates under UHV conditions.
3) Study of the growth of the subsequent layers of molecular semiconductors (pentacene, helicene, or BTB) using LEEM, STM, and XPS.

Recommended bibliography:

FAHLMAN, Mats, Simone FABIANO, Viktor GUESKINE, Daniel SIMON, Magnus BERGGREN a Xavier CRISPIN. Interfaces in organic electronics. Nature Reviews Materials. 2019, 4(10), 627-650. Dostupné z: doi:10.1038/s41578-019-0127-y.

FRANCO-CAÑELLAS, Antoni, Steffen DUHM, Alexander GERLACH a Frank SCHREIBER. Binding and electronic level alignment of π -conjugated systems on metals. Reports on Progress in Physics. 2020, 83(6). Dostupné z: doi:10.1088/1361-6633/ab7a42.

WALDRIP, Matthew, Oana D. JURCHESCU, David J. GUNDLACH a Emily G. BITTLE. Contact Resistance in Organic Field‐Effect Transistors: Conquering the Barrier. Advanced Functional Materials. 2020, 30(20). Dostupné z: doi:10.1002/adfm.201904576

Deadline for submission Master's Thesis is given by the Schedule of the Academic year 2022/23

In Brno,

L. S.

prof. RNDr. Tomáš Šikola, CSc. Director of the Institute	doc. Ing. Jiří Hlinka, Ph.D. FME dean

Summary

Deposition of organic molecules on metal substrate often results in their spontaneous arrangement driven by intermolecular and molecular-substrate interactions. This phenomenon is called self-assembly and can be used to create functional structures with atomic precision. In particular, thin films of organic semiconductors are of growing interest for their potential application in the semiconductor industry. However, the efficiency of such devices is related to the interfacial resistivity at the metal-organic interface. Therefore, the study of the growth type of organic semiconductors on metal substrates is crucial for their future applications. This diploma thesis focuses on the formation of a cover layer of well-ordered 1,3,5-benzene-tricarboxylic acid (BTB) molecules on Ag(111). The main objective of the thesis is to use this cover layer as a substrate for the subsequent growth of pentacene layers, one of the intensively studied organic semiconductors. Coverage by an ordered layer of pentacene with an area suitable for practical applications was achieved. Low-energy electron microscopy, scanning tunneling microscopy, X-ray photoelectron spectroscopy and ultraviolet photoelectron spectroscopy were used to study the growth and properties of molecular layers.

Abstrakt

Během depozice organických molekul na kovové substráty často dochází k spontánnímu uspořádání molekul vlivem mezimolekulárních a molekulárně-substrátových interakcí. Tento jev se nazývá samouspořádání a může být využit k vytváření atomárně přesných funkčních struktur. Vzrůstající zájem vzbuzují zejména tenké vrstvy organických polovodičů pro jejich potenciální využití v polovodičovém průmyslu. Efektivita takovýchto zařízení je však nevyhnutelně spojena s přechodovým odporem na rozhraní polovodiče a kovové elektrody. Studium typu růstu organických polovodičů na kovových substrátech je tak zcela zásadní pro jejich budoucí využití. Tato diplomová práce se nejprve zabývá vytvořením krycí monovrstvy substrátu Ag(111) z dobře uspořádaných molekul kyseliny 1,3,5-benzen-trikarboxylové (BTB). Hlavním cílem práce je pak použití této vrstvy jako substrátu pro růst dalších vrstvev tvořených molekulami pentacenu, což je jeden z intenzivně zkoumaných organických polovodičů. Bylo dosaženo pokrytí povrchu uspořádanou vrstvou pentacenu o rozloze vhodné pro praktické využití. Pro studium růstu molekulárních vrstev a jejich vlastností byla použita nízkoenergiová elektronová mikroskopie, skenovací tunelovací mikroskopie, rentgenová fotoelektronová spektroskopie a ultrafialová fotoelektronová spektroskopie.

Keywords

Molecular self-assembly, carboxylic acid, organic semiconductor, work function, BTB, pentacene, LEEM

Klíčová slova

Molekulární samouspořádání, karboxylová kyselina, organický polovodič, výstupní práce, BTB, pentacen, LEEM

KUGLER, D. *Growth of organic heterostructures on metal surfaces.* Brno: Brno University of Technology, Faculty of Mechanical Engineering, 2023. 66 s. Supervised by Ing. Pavel Procházka, Ph.D.

I hereby declare that I have written my master's thesis on the theme of *Growth of organic heterostructures on metal surfaces* under the supervision of Ing. Pavel Procházka, Ph.D., and using the literature and other sources of information which are all properly quoted in the thesis and detailed in the list of literature at the end of the thesis.

Bc. David Kugler

My thanks go to Ing. Pavel Procházka, Ph.D., for his guidance, patience in solving problems in the laboratory and helping in data analysis. Then I would like to thank Dr. Matthias Blatnik for his help in measuring UPS and evaluating the results and Dr. Zdeněk Jakub for his help in optimizing the cooling solution of the STM. I would also like to thank doc. Jan Čechal, Ph.D. for explanation of all the unclarities I encountered while writing this thesis.

CzechNanoLab project LM2023051 funded by MEYS CR is gratefully acknowledged for the financial support of the measurements/sample fabrication at CEITEC Nano Research Infrastructure.

Bc. David Kugler

Contents

1. Introduction

One of the possibilities considered for electronic miniaturization is the use of organic semiconductors. Organic materials have already proven their application potential in OLED (Organic Light-Emitting Diode) technology in the past decades and their electronic properties are now being intensively investigated. For their application in current electronics, it is necessary to use metal electrodes and to create a metal-organic interface, whose formation and properties need to be precisely characterized. The ultra-high vacuum (UHV) offers the ideal conditions for real-time in-situ study of metal-organic interface formation, where very low and well-defined coverages with almost no contaminants present can be achieved. Moreover, a self-assembly phenomenon that allows organic molecules to self-organize into well-defined structures often occurs on the metal surface. In this way, the physical properties of one layer thick organic materials can be precisely investigated.

The interfacial metal-organic charge transfer efficiency reflects the energy level misalignment. If it is high, high voltage needs to be applied to achieve charge transfer, which fundamentally reduces the efficiency and lifetime of the devices. Therefore, several ways to modify the work function of the substrate and thus reduce the contact resistance are being investigated. One of the intensively studied possibilities is surface passivation with self-assembled monolayers [1].

Countless studies have already been published on the topic of homogeneous and heterogeneous organic monolayers [2, 3]. However, due to their complexity, heterogeneous multilayers are still at the beginning of the research. It is the complexity provided by multilayers that would be important in the future for the selection of suitable molecular systems for application in the semiconductor industry. We are focusing on one such system in this thesis.

Our goal is to study the growth of the intensively researched organic semiconductor, pentacene, on the Ag(111) single crystal surface. Moreover, the influence of the pentacene layer on the work function of the substrate is investigated. Previous research found that the first pentacene layer does not form an ordered structure on the Ag(111) surface at room temperature [4, 5, 6]. Instead, it exists on the surface as a two-dimensional (2D) molecular gas. That is why we first cover the substrate with a well-ordered layer of 4,4',4"-benzene-1,3,5-triyl-tribenzoic acid (BTB) molecules, which aims to modify charge transfer properties and growth type of subsequent pentacene layers. In addition, we aim to measure the effect of this cover layer on the substrate work function.

The first two chapters of the theoretical part deal with the growth of molecular layers and the phenomenon of self-assembly. Subsequently, the influence of molecular layers on the electronic properties of the substrate is explained. The current state of the art of investigated molecules is also summarized. The last chapter of the theoretical part describes the principle of devices used to monitor the growth and characterization of molecular layers.

At the beginning of the experimental part, the cleaning of the metal crystal and the preparation of the cover layer formed by BTB molecules are presented. Subsequently, the growth of pentacene layers on this cover layer is described in detail. The grown pentacene layers are then characterized using several methods. Finally, work function values after each step of the system preparation are presented and changes in work function between individual steps are discussed.

2. Theoretical part

2.1. Growth of molecular layers

This thesis focuses on the growth of organic semiconductor layers on a molecular monolayer of carboxylic acid covering a metal substrate. The growth and characterization of such molecular layers require an inert environment in which the transport of molecules and the growth of molecular layers will be minimally affected by particles in the surrounding environment. The best such environment we can create is an ultra-high vacuum (UHV). However, even in UHV conditions there are residual particles that will adsorb on the surface of our substrate over time and thus contaminate it. Therefore, it is necessary not only to clean the surface of the substrate but also to minimize its defects so that we can create well-defined molecular layers. Ion sputtering and annealing cycles are the most commonly used for metal substrates within the UHV conditions. The surface thus prepared is suitable for the growth and investigation of molecular layers. [7].

2.1.1. Deposition of the molecules

A bottom-up approach is exclusively used to create molecular layers. It involves depositing the material on the substrate and then arranging it into the desired structure. Depending on the nature of the deposited material, there are several ways of depositing the material directly in UHV conditions. Molecular layers are almost exclusively grown using organic molecular beam epitaxy (OMBE), which allows epitaxial growth of deposited material on the substrate. Its biggest advantage is the stable deposition rate, which can be precisely controlled by deposition temperature [7].

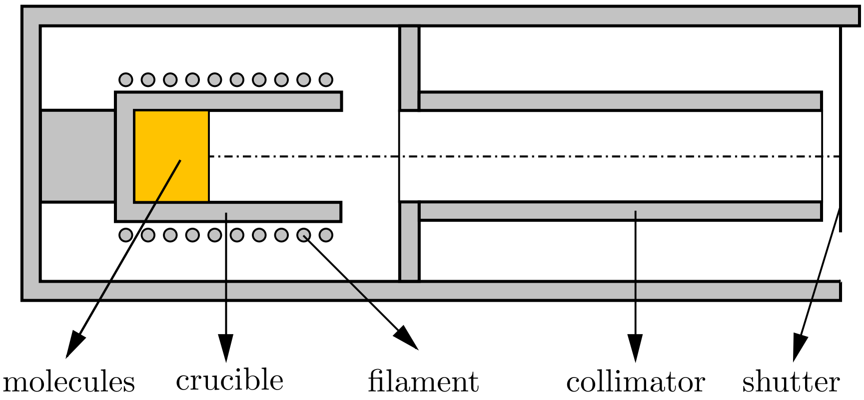

Figure 2.1: Schematic of an effusion cell used for OMBE. Modified from [7].

OMBE works on the principle of evaporating the desired material and then condensing it on a clean substrate. The molecules are contained in a crucible placed in an effusion cell. The crucible is heated, most often by passing a current through a surrounded tungsten filament, which increases the evaporation rate of the molecules. The molecules flow through the collimator, which forms the molecular beam to the dimensions of the sample, and condense on the surface of the substrate. A shutter at the end of the collimator regulates the transport of molecules to the substrate, allowing us to precisely control the deposition time. To maintain a constant flow of molecules, the shutter needs to be open only when the temperature of the crucible has stabilized at desired deposition temperature [7, 8].

2.1.2. Atomic processes

The deposition of molecules on a substrate is a thermodynamically non-equilibrium process. In the case of thermodynamic equilibrium, the number of adsorbed molecules equals the number of desorbed molecules, the number of attached molecules to the molecular islands equals the number of detached molecules from the molecules islands, and so on. However, we require that adsorption outweighs desorption for the growth of a molecular layer. All surface processes follow Boltzmann statistics, and their probability is determined by the activation energy E and thermodynamic temperature T as

$$P \propto e^{-\frac{E}{kT}}, \tag{2.1}$$

where k is Boltzmann's constant. The condensation of molecules on the surface is determined by the so-called impinging rate, or the number of particles impinging per unit of surface per unit of time, according to the relation

$$F = \frac{p}{\sqrt{2\pi m k T_{\mathrm{S}}}}, \tag{2.2}$$

where p is the partial pressure of the impinging particles, m is the molecular weight of the particles and T_{S} is the source temperature. However, not all incident molecules are necessarily adsorbed, which is expressed by the sticking coefficient s in relation to the adsorption rate r_{a}

$$r_{\mathrm{a}} = sF. \tag{2.3}$$

The sticking coefficient takes values from 0 to 1 and is influenced by the surface coverage function, which represents the probability of finding a suitable adsorption site.

Once the molecules have condensed on the surface, they may re-evaporate instantaneously, adsorb to a given site, or diffuse across the surface. The system seeks to minimize its free energy by adsorbing molecules at favorable sites to which the molecules must first diffuse. Diffusion is described as random-walk motion, which is explained as the random hopping of molecules between adjacent adsorption sites. This hopping process has a mean-square distance $\langle r \rangle$ in time t given by

$$\langle r \rangle = \nu a^2 t, \tag{2.4}$$

where ν is the frequency of hops and a is the hop distance. Mean-square distance per unit time is known as the diffusion coefficient D

$$D = \frac{\langle r \rangle}{zt} = \frac{\nu a^2}{z}, \tag{2.5}$$

where z is the number of neighboring sites which the molecules can hop. For square surface atom arrangement, $z = 4$ and for hexagonal surface atom arrangement, $z = 6$. Since some activation energy must be overcome for these hops to occur, it is a thermally activated process. The activation energy of diffusion is much lower than the activation energy of desorption. If the activation energy of diffusion is less than kT, the molecules move relatively freely across the surface in the form of a two-dimensional (2D) molecular gas [7, 8].

Adsorption can take place in several ways. In the first place, the adsorption of molecules occurs on surface defects such as atomic step-edges. The second way is that several molecules collide and form bonds with each other during diffusion over a surface, resulting in the formation of nuclei. These small nuclei are only stable for a short time and very quickly decay again. However, if enough molecules attach to them before they break up, the nuclei exceed a certain critical size and become stable, making it a molecular island. Other molecules can then attach on the edges of these stable islands [7, 8, 9].

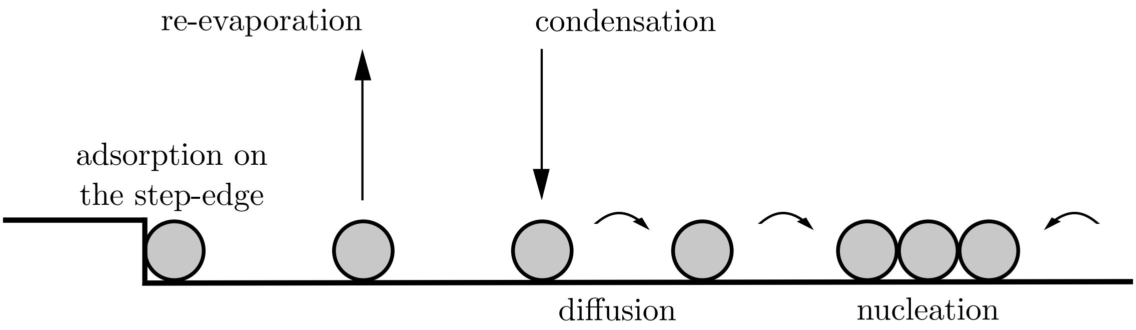

Figure 2.2: Schematic of atomic processes. Modified from [8].

2.1.3. Growth of molecular layers

Based on the processes described above, the growth of molecular layers can be divided into several regimes. At the beginning of the deposition in the nucleation regime, the first molecules reach the surface, but there are no favorable adsorption sites except for defects. Therefore, molecules migrate over the surface and collide, resulting in the nucleation of the first nuclei. As the concentration of molecules increases, the frequency of their collisions also increases, resulting in the formation of the first stable islands. At the moment when the probability of a molecule joining existing island is equal to the probability of forming new nuclei, we can start talking about the intermediate-coverage regime. In this regime, the number of diffusing molecules on the surface peaks. At the point where the mean free path of the diffusing molecule is the same as the mean distance between the islands, the growth of the existing islands is already taking place and this phase is called the aggregation regime. In the last phase of growth, the so-called coalescence regime, the molecular islands merge [7].

The shape of the molecular islands during deposition is affected by the ability of the newly adsorbed molecules to diffuse around the edge of the island. This ability can be influenced by the temperature of the substrate. If the molecules can diffuse along the island edges and find the most energetically favorable adsorption sites, the growth of compact islands occurs. However, if diffusion does not occur or is very limited (typically at low temperatures), growth in non-compact, dendritic, irregular shapes occurs. [7].

Based on the surface free energy, which is the energy required to create an additional piece of surface or interface per unit area, the growth of molecular layers can be divided into three modes. For this purpose, we denote the surface free energy of the vacuum-substrate interface as γ_{S}, the surface free energy of the vacuum-molecular layer interface as γ_{M}, and the interface free energy between the substrate and the molecular layer as $\gamma_{\mathrm{S-M}}$. In the case that

$$\gamma_{\mathrm{S}} < \gamma_{\mathrm{M}} + \gamma_{\mathrm{S-M}}, \tag{2.6}$$

it is more energetically advantageous for the molecular layer to grow in the form of 3D molecular islands and we call this island mode (Figure 2.3a). In the case that

$$\gamma_{\mathrm{S}} \geq \gamma_{\mathrm{M}} + \gamma_{\mathrm{S-M}}, \tag{2.7}$$

it is more energetically advantageous for the molecular layer to first cover the entire substrate surface, and only after that the next layer starts to grow. We call this growth mode layer-by-layer (Figure 2.3c). A combination of these two modes is the layer-plus-island mode when the substrate is first covered by a monolayer of molecules and then 3D islands start to grow on top of this layer (Figure 2.3b). This occurs when there is an elastic strain caused by lattice mismatch between the substrate and the deposited molecular layer [8].

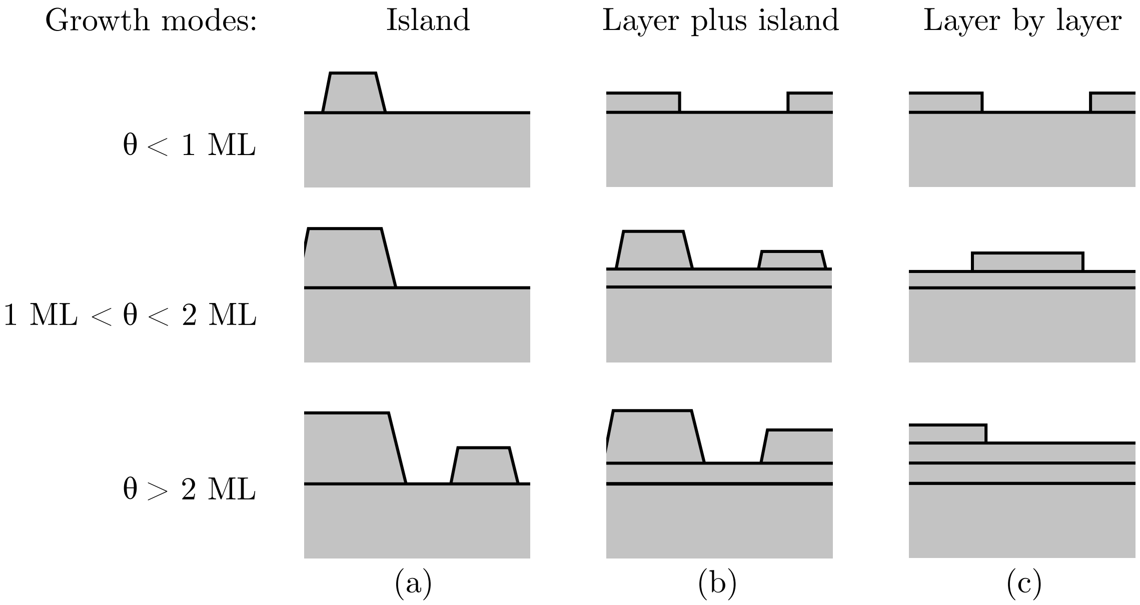

Figure 2.3: Schematic of the growth modes. The amount of deposited material is shown in the picture description on the left. It is given in the number of monolayers (ML) and is denoted by θ. Modified from [7].

2.2. Molecular self-assembly

Deposition of molecules under UHV conditions does not guarantee the growth of long-range ordered structures. However, in the case of many molecular systems, a phenomenon called self-assembly occurs. As the name suggests, it is the spontaneous arrangement of the basic building blocks, in this case, organic molecules, into regular patterns and structures. This phenomenon is not driven by any external force; it is the result of the system's effort to reach the most energetically favorable state. The main parameter affecting the self-assembly and the form of the resulting structure are intermolecular and molecular-substrate interactions. Intermolecular interactions should not be too weak, as this would lead to the impossibility of forming bonds and stable structures under non-equilibrium conditions when the deposition takes place. On the other hand, the formation of strong covalent bonds would mean the impossibility of bond breaking, which is necessary to achieve the equilibrium structure. The shape of the resulting structure is also influenced by interactions between the molecules and the substrate. If they are strong, the resulting structure is influenced by the symmetry of the substrate. In the case of weak molecular-substrate interactions, the resulting structure can be relatively independent of the substrate [10, 11].

For self-assembly to occur, not only interactions have to be considered, but also deposition conditions. If the deposition temperature and associated flux F of molecules is too high, molecules may fail to diffuse to the energetically most favorable states and they remain trapped in the diffusion-limited state. However, if the deposition takes place near equilibrium conditions, molecules have enough time to diffuse to the most energetically favorable adsorption sites and form the equilibrium structure [10, 11].

Given an overwhelming amount of chemical and geometric structures of various organic molecules serving as basic building blocks, it is clear that the self-assembly process allows us to design a huge amount of molecular patterns. Concerning the dimensions of individual molecules, self-assembly provides a completely new possibility to create functional structures with atomic precision. The possibilities of exploiting this fact will be discussed in more detail in the following chapters [2, 3, 10, 12].

2.2.1. Interactions contributing to self-assembly

To create the structures of desired shapes, a detailed understanding of the individual interactions that contribute to the self-assembly process is essential. In the following paragraphs, we summarize the most important interactions that are relevant to the system we are concerned with in this thesis. We start from the weakest interactions and gradually get to the stronger ones.

Van der Waals forces

Van der Waals (vdW) forces are long-range attractive forces occurring in all systems, which act both between individual molecules and between molecules and the substrate. They are arising from the interaction between an instantaneous dipole of the molecules and an induced charge fluctuation in the metal. vdW interactions are isotropic and non-selective. The more atoms a molecule contains, the stronger the vdW interactions can be. In the case of systems of large molecules in which stronger interactions do not occur, vdW interactions determine the resulting structure. In all other cases, they only subtly contribute to the balance of other interactions [2, 3].

Hydrogen bonding

Hydrogen bond is one of the most important bonds between organic molecules, especially carboxylic acids. It is related to the uneven distribution of charge in the molecule due to the bond between hydrogen and another, highly electronegative atom (typically oxygen or nitrogen). A more electronegative atom partially attracts the electron pair forming the bond with hydrogen, causing a partial positive charge on the hydrogen and a partial negative charge on the more electronegative atom. Opposite partial charges on the atoms of different molecules can attract each other and form bonds. The hydrogen bond is strong enough to form a stable network, but it also allows bond breaking and rearrangement of molecules until an equilibrium structure is formed. Due to its directionality, hydrogen bonding is often used to design molecular networks [2, 3].

Interactions of π-electrons

Although some of the π-electron interactions can be classified under vdW interactions, we mention them separately because of their importance for the system we are studying. These interactions occur most often between aromatic molecules that are rich in π-electrons. The highest probability of occurrence of electrons forming a π-bond is above and below the plane of the molecular backbone formed by σ-bonds. Because of this, π-electrons are close to the substrate after the adsorption of the molecules, which increases the probability of their interaction with the substrate. In the context of molecular design, π-electrons ensure the flat-like adsorption of the molecules to the surface. Conversely, π-electrons of adjacent molecules repel each other, which can result in ABAB stacking (Figure 2.5a) or standing-up molecular arrangement (Figure 2.5b) [2, 14].

Other types of interactions

In addition to the interactions described above, there are others that are not relevant to the system we are studying. As an example, metal-organic bonds play a crucial role in systems where metal adatoms are deposited on the surface in addition to the organic molecules. The strongest bond is the covalent bond. While it allows the formation of molecular structures, it prevents bond breaking in most of the molecular systems, leading to more irregular patterns [3].

2.2.2. Growth beyond the first monolayer

For a long time, single-component monolayer systems were the main area of interest for scientists, providing insight into the mechanisms of molecular self-assembly and allowing a good description of the influence of individual interactions on the resulting structure. Recently, research has been extended also on self-assembled monolayers consisting of two or more components [2, 3]. Assembling such monolayers from multiple components gives more possibilities both for achieving structures of desired shapes and in terms of tuning electronic properties (more on this in the next chapter).

However, only a few studies have focused on the atomic scale view of the subsequent layers of self-assembled organic molecules, which will be crucial for future applications in the organic semiconductor industry. Therefore, in this thesis, we will focus on the growth of an organic semiconductor (OS) layer on a pre-prepared, well-defined monolayer consisting of self-assembled carboxylic acid molecules. We assume that such a system is suitable for the initial study of multilayer growth behavior [2, 3].

In the case of the growth beyond the monolayer, we must anticipate several differences from the growth of the first layer on a metallic substrate. The biggest change here is that the second layer will no longer be in direct contact with the substrate. In the case of organic molecules containing phenyl rings, π-electrons of these molecules will not hybridize the metallic states of the substrate. Instead, they will interact with the π-electrons of the molecules forming the first layer, or with the π-electrons of other molecules in the second layer, which may lead to unexpected types of growth. In the following paragraphs, we will show some examples.

Example of growth – single component multilayer
In the study of α-Sexithiophene (α-6T, Figure 2.4a) on Au(100), it became apparent that even the growth of multilayers from a single component can be quite complicated. The first layer of molecules adsorbed on the substrate as expected, i.e. flat-like (Figure 2.4b). The second layer of molecules was shifted compared to the first layer, so the molecules did not lie exactly on top of each other. Moreover, the molecules did not adsorb flat-like, but in a certain alternating tilt with respect to the substrate and the first layer, in a so-called staggered molecular arrangement (Figure 2.4c). The principle of the arrangement of this layer began to resemble the α-6T(010) bulk structure, but the values of the shift and tilt between the layers were different. The arrangement of the third layer of molecules then further approached the bulk structure. From this observation, it was proposed that together with the increasing distance of the molecules of the other monolayers from the surface and thus decreasing influence of the substrate, the arrangement of the molecules gradually changes, converging to a bulk structure for the cases of the higher layers [13]

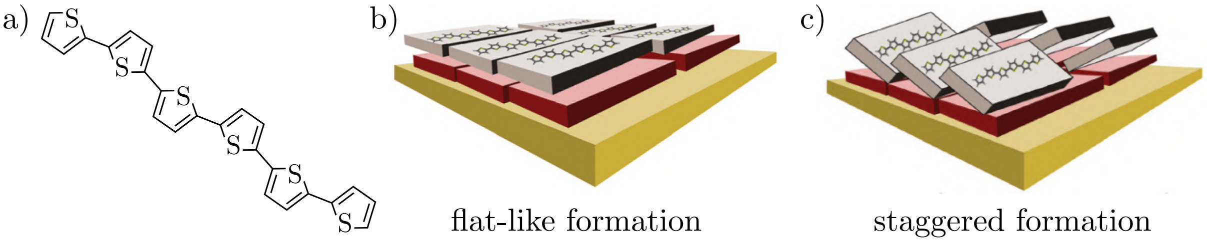

Figure 2.4: (a) Chemical structure of α-6T. (b) Schematic of flat-like adsorption and (c) proposed staggered formation. Taken from [13].

Example of growth – pentacene on graphene
The growth of pentacene (Figure 2.5a) on graphene prepared by chemical vapor deposition on SiO_2 substrate has also been studied. As-grown graphene films were covered with a layer of polymethylmethacrylate (PMMA), which served as a support for graphene transfer. This PMMA layer is then almost removed by reactive ion etching and the concentration of its residues is subsequently decreased by annealing. However, it has been shown that if the final annealing of the sample and thus removal of PMMA residues do not occur, pentacene shows different growth on pure graphene and these residues.

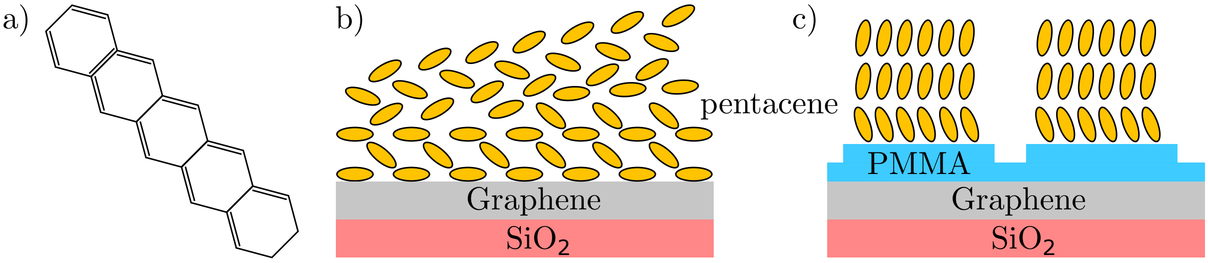

Figure 2.5: (a) Chemical structure of pentacene. (b) Schematic of pentacene growth on the clean graphene and (c) PMMA residues. Modified from [14].

Indeed, the π-electrons of pentacene interact with the graphene surface, leading to epitaxial flat-like growth in the case of the first layer. Subsequent layers are then alternately tilted with respect to the substrate, forming so-called ABAB stacking (Figure 2.5b). Growth of the subsequent layers is caused by the π-electrons trying to avoid each other. However, when pentacene grows on PMMA, π-electrons do not interact with the substrate or the PMMA residue. Pentacene molecules adopt a standing-up orientation, which means that they grow almost vertically, right from the first layer (Figure 2.5c) [14].

2.3. Energy level alignment

So far, we have only been concerned with the transport of molecules to the substrate, the growth of molecular islands, and ideally the simultaneous molecular self-assembly process. The interactions of π-electrons and their influence on the resulting structure were mentioned. This was no coincidence, as molecules containing π-electrons, so-called π-conjugated molecules, are currently under intense research for their potential use in organic electronics. Organic semiconductor (OS) based electronics have experienced rapid development in recent years, with organic light-emitting diode (OLED) displays, organic photovoltaic (OPV) cells, and organic field-effect transistors (OFETs). The lifetime and performance of these devices critically depend on the electronic properties of the interfaces between the different materials [1, 15, 16].

Therefore, we now look at how the adsorption of π-conjugated molecules affects the electronic properties of the metal substrate. To do this, we need to define the most important quantities and energy levels occurring at metal-organic interfaces.

2.3.1. Energy diagram of a metal substrate

Let us first consider a pure metal substrate before the deposition of organic molecules. A continuum of electronic states occurs in the metal, which is occupied up to the Fermi level or Fermi energy ($\mathrm{E_F}$). One of the most important electronic properties of any material is the work function (WF or ϕ), which is given by the energy difference between $\mathrm{E_F}$ and the vacuum level (VL). This difference represents the energy required for an electron to escape from $\mathrm{E_F}$ in the metal into the vacuum. The existence of WF is simple. The surface of the metal is a bulk termination that causes a non-uniform charge distribution in space. One can imagine that the electron cloud partially leaks from the metal surface into the vacuum, but there are no positive ions. Because of this, there is an excess of electrons above the surface, which in turn are missing in the bulk, creating a so-called surface dipole. This dipole is directed into the bulk and contributes to the work function of the material together with the bulk chemical potential. The higher the surface dipole, the higher the work function [3, 15].

The work function is a property of the surface and depends on many factors. First of all, it is the chemical composition of the substrate and the crystal plane that determines the compactness of the surface. The more compactly the surface atoms are arranged, the higher the work function. It also depends on the oxidation state of the surface, its purity, and the concentration of surface defects.

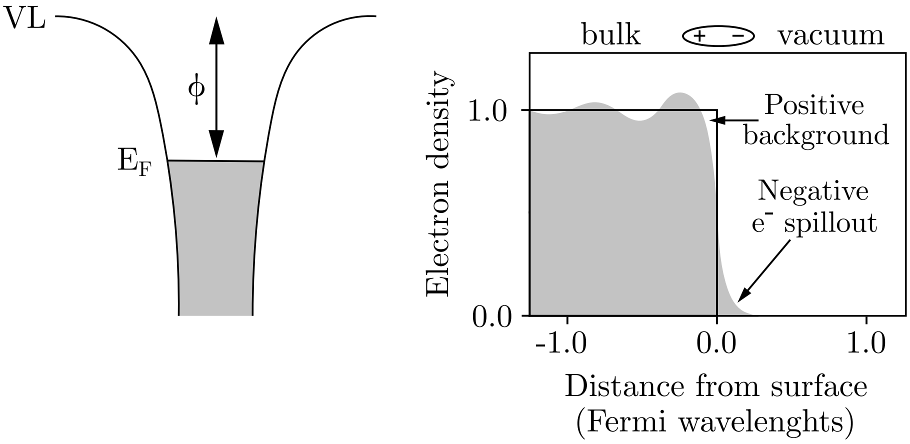

Figure 2.6: (a) Energy diagram of a clean metal substrate. (b) Schematic of the dependence of electron density on the distance from the surface. Modified from [3].

2.3.2. Energy levels of π-conjugated molecules

As mentioned at the beginning of this chapter, attention has been paid to π-conjugated molecules. Conjugated means that they periodically alternate between single and double bonds, which typically occurs for molecules consisting of phenyl rings. This is due to sp^2 hybridization of the carbon atoms, which results in single σ-bonds forming the backbone in the plane of the molecule, whereas the p_z electron orbital is highly delocalized, allowing them to overlap with the orbitals of neighboring atoms to form π-bonds. The most important energy levels of molecules are the highest occupied molecular orbital (HOMO) and the lowest unoccupied molecular orbital (LUMO). The energy difference between VL and HOMO is called ionization potential (IP) and the energy difference between VL and LUMO is called electron affinity (EA) [3, 15, 16, 17].

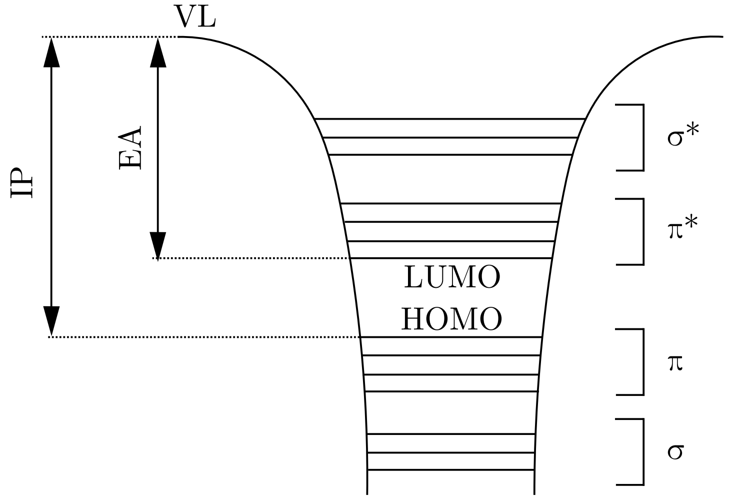

Figure 2.7: Energy levels of π-conjugated molecules. π- and σ-orbitals are occupied, π^*- and σ^*-orbitals are unoccupied. Modified from [16].

2.3.3. Metal-organic interface

In the case of the adsorption of π-conjugated molecules on metal surfaces, several phenomena may occur. First, Pauli's repulsion between the electrons in the molecule and the electron cloud leaking from the metal into the vacuum causes a partial push of this electron cloud back into the substrate, reducing the surface dipole and thus decreasing the work function. This is called the push-back effect, it occurs in all systems, and the magnitude of this effect depends on the vertical distance between the surface and the adsorbed layer. In addition, the intrinsic dipole moment of the adsorbed molecules can contribute to the total surface dipole, which can generally decrease or increase the surface dipole. Finally, there may be electron transfer between the molecular layer and the substrate, which also alters the surface dipole [3].

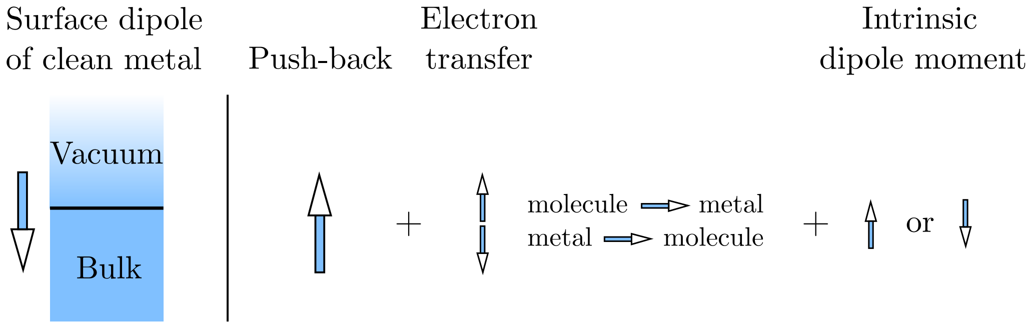

Figure 2.8: Individual contributions to the surface dipole. Modified from [3].

All these effects add up and ultimately change the energy level alignment (ELA) of the system. This change is dependent on the surface coverage of the molecular layer. Importantly, mainly the first layer of adsorbed molecules typically contributes to the change in dipole moment and hence the WF. Any additional layers of the same molecules change the WF only if their adsorption changes the arrangement of the first layer of molecules. If we deposit a second layer of molecules on a substrate covered by a monolayer of other molecules, the surface dipole may change again [3].

Two types of charge transfer may occur at the interfaces between organic molecules and the metal substrates. The first type occurs during chemisorption, i.e. in systems with strong molecular-substrate interactions. In this case, partial charge transfer occurs through bonds between the molecules and the substrate. Within the system studied in this thesis, partial charge transfer occurs in the case of deprotonation of carboxylic groups and the subsequent formation of bonds with substrate atoms (more on deprotonation in the next chapter). The second type of charge transfer is called integer charge transfer (ICT). In this case, integer multiples of charge are transferred between molecules and the substrate, usually by electron tunneling. An example of the system where ICT occurs is the deposition of molecules on a metal substrate covered with a thin non-conducting layer through which electrons can tunnel. We will describe the mechanism of this type of charge transfer in more detail, but first, we need to understand the processes during the adsorption of molecules [15].

The adsorption of molecules on the surface leads to the electronic and geometric relaxation of the molecules. This manifests itself in a shift in the positions of HOMO and LUMO, in their broadening, and also in the formation of self-localized states called polarons. It means that HOMO and LUMO energy levels extend to the energy values between them. To simply explain the conditions for ICT, we denote as HOMO-c the critical energy value to which the initial HOMO of unrelaxed molecules has broadened. In the same way, we denote as LUMO-c the critical energy value to which the initial LUMO of unrelaxed molecules has broadened. In the case where HOMO-c is above the E_F after the adsorption of the molecules, electron tunneling occurs from the molecules to the unoccupied states of the substrate above the E_F (Figure 2.9a). The electron tunneling occurs until the E_F and HOMO-c values are equal. The consequence of the tunneling of electrons from the molecule to the substrate is that the molecules become positively charged, whereas the substrate becomes negatively charged, making a dipole that decreases VL and WF. If E_F of the metal is between HOMO-c and LUMO-c, no charge transfer occurs (Figure 2.9b). In the latter case, if LUMO-c is below E_F, electron tunneling occurs from the metal to the unoccupied states of the molecules (Figure 2.9c). Tunneling occurs again until the values of E_F and LUMO-c are equal. The consequence of electron tunneling from the metal to the molecules is that the molecules become negatively charged, whereas the substrate becomes positively charged, making a dipole that increases VL and WF. [15].

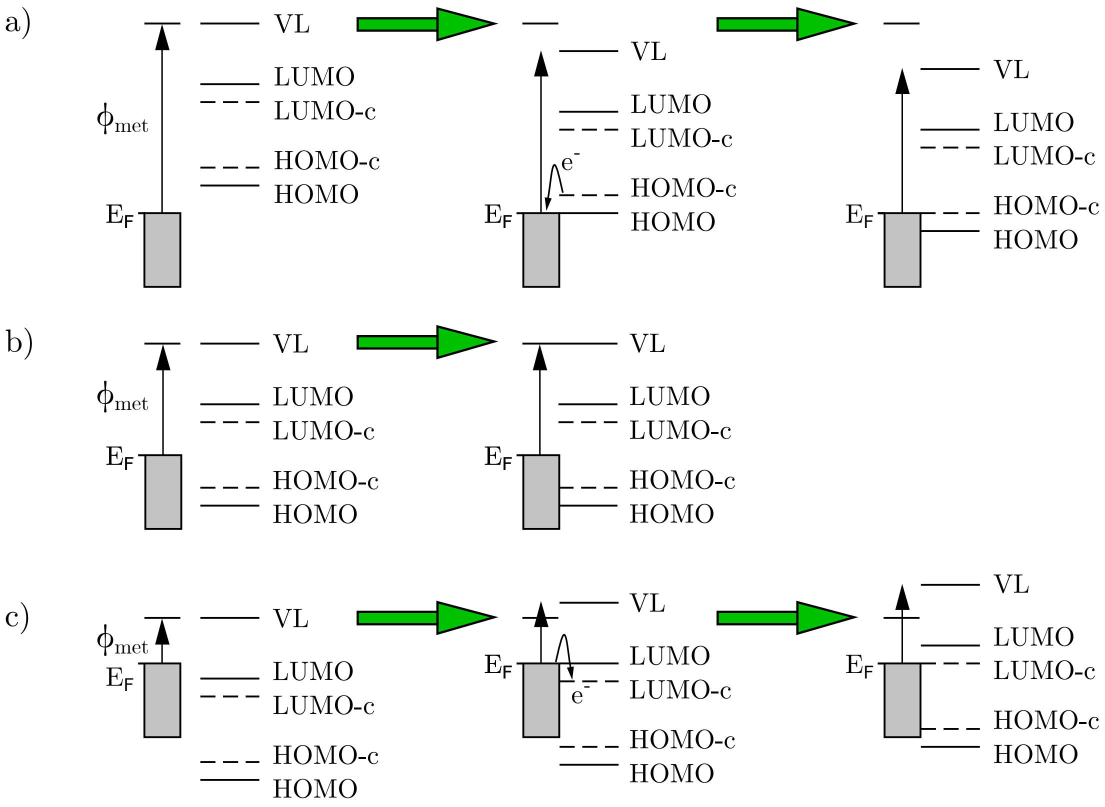

Figure 2.9: Schematic of three different cases of ELA. (a) In the case where HOMO-c is above E_F after adsorption of the molecules, electrons tunnel from the molecules to the unoccupied states above E_F of the substrate, which decreases the surface dipole and WF. (b) In the case where E_F is between HOMO-c and LUMO-c after adsorption of the molecules, there is no tunneling of electrons. (c) In the case where LUMO-c is below E_F after the adsorption of the molecules, electrons tunnel from the sample to the unoccupied molecular orbitals, which increases the surface dipole and WF. Modified from [15].

As explained in the previous paragraphs, the adsorption of molecules on the surface induces a shift of VL and thus changes the work function of the substrate. For efficient charge transfer, it is not desirable that the difference between the WF of a metal and IP (so-called hole-injection barrier) or EA (so-called electron-injection barrier) of an organic semiconductor is as high as in the case of direct adsorption of the OS on the sample surface. In the case of a high injection barrier, a high contact resistance R_c must be overcome for charge transfer. In practical applications, this requires the application of high voltage, which reduces the efficiency and lifetime of a device. Therefore, reducing R_c is a major challenge in the organic semiconductor industry. Due to the aforementioned VL shifts during the adsorption of molecules, the WF of a metal and IP (or EA) of an organic semiconductor cannot be simply compared to determine the injection barrier after the molecules of the OS are adsorbed on the metal substrate [1, 3, 16].

In this thesis, we investigate the covering (passivation) of a metal substrate with a monolayer of well-ordered organic molecules that changes the work function and at the same time influences the growth of subsequent organic semiconductor layers. Such a cover layer, which serves to reduce the energy level misalignment between the metal and the OS, is called a charge-injection layer (CIL) [1, 16, 18].

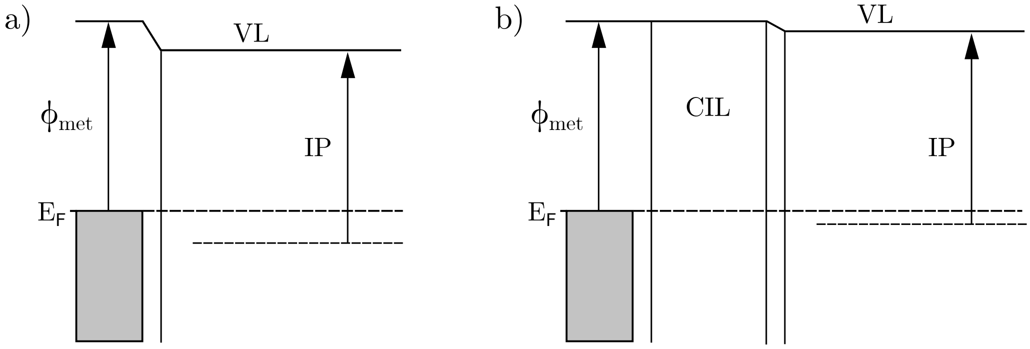

Figure 2.10: Schematic of the energy level misalignment between (a) a pure and (b) passivated substrate and IP of a deposited OS. A change in WF due to the passivation of the surface with a cover layer may lead to a reduction of the injection barrier between the (passivated) substrate and OS. Modified from [16].

2.4. Investigated molecules

Carboxylic acid molecules may be suitable precursors for use as charge-injection layers. They contain one or more -COOH functional groups allowing the formation of hydrogen bonds between other carboxylic groups of the surrounding molecules on metal surfaces. In the case of two carboxylic groups of different molecules, it is common that a pair of hydrogen bonds is formed between them (Figure 2.11a). This pairwise interaction is relatively strong and highly directional. Increasing the temperature of the system often results in deprotonation (i.e., loss of hydrogen) of the carboxylic groups, thereby fundamentally changing the binding properties of the molecules. This changes the work function of the system and causes spontaneous rearrangement of the molecules on surfaces [12, 19, 20, 21].

For the molecules, to cover the entire surface and serve as a CIL, it is usually advisable that its backbone be composed (at least partially) of phenyl rings to maximize the probability of flat-lying configuration of the molecules on the metal substrate [22]. π-electrons also mediate molecule-substrate interactions and, in the case of deposition of a second layer on this CIL layer, influence the growth of the second layer.

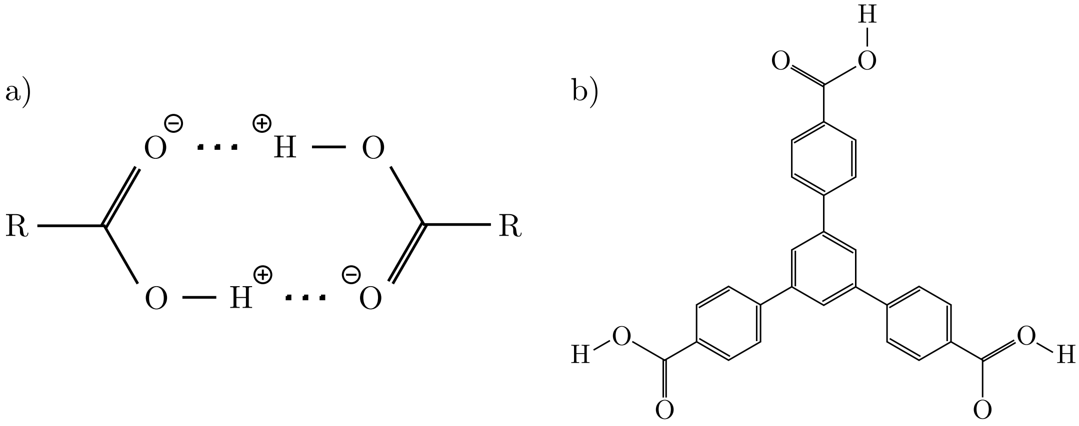

Figure 2.11: (a) Schematic of a pair of hydrogen bonds between two carboxylic groups. (b) Chemical structure of BTB.

2.4.1. BTB

In this thesis, we will use 4,4',4"-benzene-1,3,5-triyl-tribenzoic acid (BTB) as the basic building block of the CIL. The molecule consists of three 4-benzoic acid groups arranged around a central benzene core, giving the molecule a 3-fold symmetry (Figure 2.11b).

Previous research showed that this molecule adsorbs in a flat-lying configuration on the Ag(111) substrate to form a hexagonal network at room temperature [23]. Each of the hexagons is made up of six BTB molecules, which are interconnected by double hydrogen bonds (Figure 2.12a). Gentle annealing to a temperature of 320 K induces deprotonation of one third of the carboxylic groups, leading to the rearrangement of the molecules into a more compact chain structure. Within one chain, three carboxylic groups from (three different) molecules meet, with the middle carboxylic group being deprotonated. As a result, the outermost two molecules are linked to this carboxylate residue by a single hydrogen bond (Figure 2.12b). Further annealing to a temperature of approximately 420 K leads to deprotonation of the second third of carboxylic groups, which induces rearrangement into a close-packed 2D layer. In this case, one third of carboxylic groups remain protonated, but the resulting arrangement no longer involves hydrogen bonds (Figure 2.12c). Under equilibrium conditions, all three phase arrangements are stable and well-defined [23].

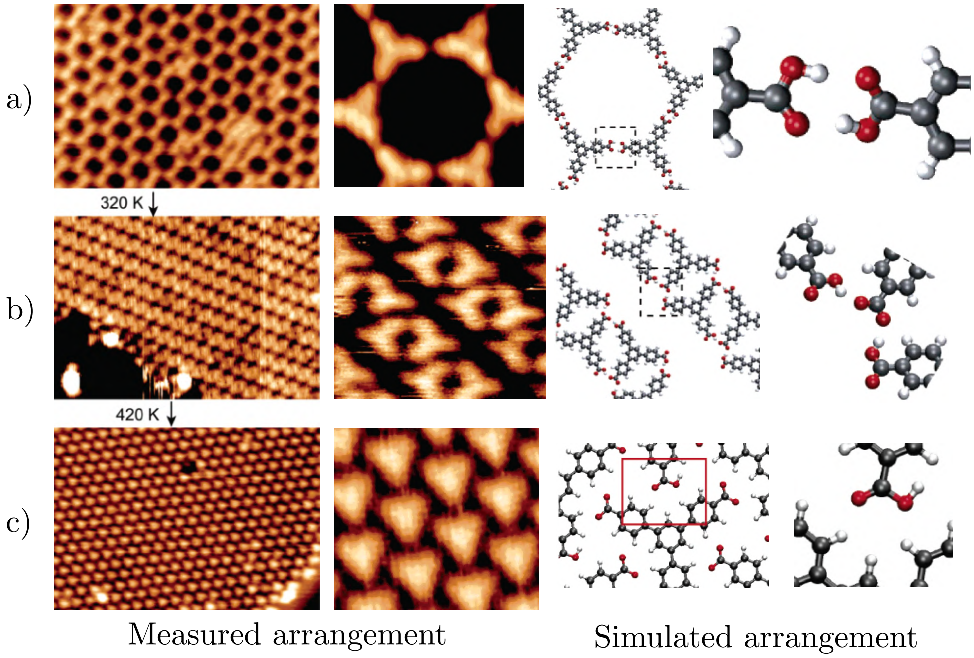

Figure 2.12: Three different arrangements of BTB molecules on Ag(111) surface. In the left column are real images measured by STM, in the right column are atomistic models of individual arrangements. Taken from [23].

The different phases of the BTB molecules have continued to be investigated on other substrates. BTB has been shown to form a hexagonal structure even on a graphene/Ir(111) substrate [24]. The latter served as a host molecule for the deposition of guest-molecule cobalt phthalocyanine (CoPC). These are bound randomly to one of six adsorption sites within the hexagons formed by BTB (Figure 2.13a and 2.13c). In the case of higher CoPC coverage, two of these molecules bound across within a single hexagon formed by BTB, distorting the hexagonal structure (Figure 2.13b and 2.13d). The structure showed considerable elasticity as the positions of the CoPC molecules within each hexagon changed during the annealing and subsequent cooling of the system. However, the hexagons remained compact and closed [24].

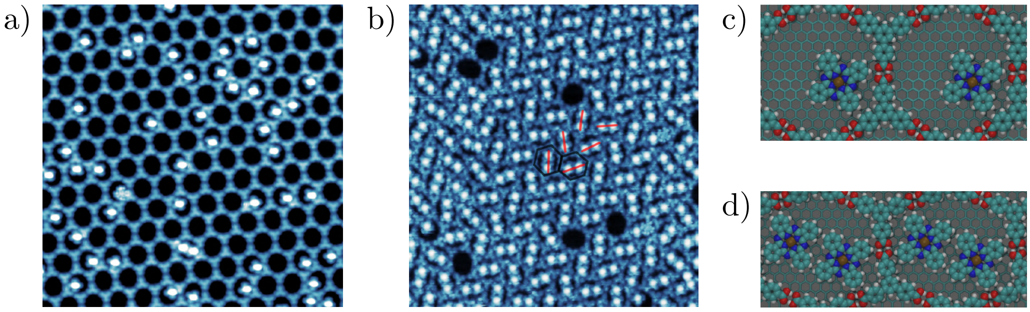

Figure 2.13: (a) and (b) STM images of the hexagonal arrangement of BTB molecules serving as a host system for CoPC molecules. (c) and (d) Atomistic model showing CoPC molecules inside the hexagons formed by BTB molecules. Taken from [24].

Intensive research on the BTB molecular monolayer has also been conducted at the liquid-solid interface, specifically at the interface of heptanoic (7A), octanoic (8A), and nonanoic (9A) acid (serving as solvents for BTB) solutions with highly oriented pyrolytic graphite. Depending on the solvent, BTB molecules formed either the hexagonal structure (8A and 9A) or a densely packed row structure (7A) at room temperature. During subsequent annealing of BTB solution systems, the hexagonal structure formed from 8A and 9A solutions transforms into a densely packed row structure at different temperatures and this transformation is reversible [25]. It was also shown that decreasing the concentration of BTB in 7A solution leads to the formation of the hexagonal structure [25, 26]. Spontaneous rearrangement of BTB molecules between hexagonal structure and chain structure has been also observed based on the polarity of the voltage applied during scanning tunneling microscope measurements of the sample [27]. Only in the case of the deposition of BTB molecules on the Ru(0001) substrate, none of the aforementioned long-range ordered formations were observed [28].

Previous research has shown that the BTB molecule forms several well-defined ordered phases. These could serve as charge-injection layers. To accurately describe the effect of this layer on the energy-level alignment between the metal substrate and the organic semiconductor, we decided to use pentacene as the OS, which is one of the most intensively studied OS ever due to its high hole mobility [6].

2.4.2. Pentacene

Unlike BTB, pentacene molecules contain no functional groups (Figure 2.5a) and interact with the substrate and other molecules mainly via π-electrons. Its growth and electronic properties have been investigated in detail in many papers, in the following paragraphs only the most important findings will be summarized.

In several papers, it is declared that at room temperature the first layer of pentacene deposited on Ag(111) occurs on the surface as a highly mobile 2D molecular gas [4, 5, 6]. This was confirmed by low-energy electron diffraction (LEED) even at 78 K (Figure 2.14a) [6]. However, when the sample was cooled after deposition to 50 K, long chains of ordered, flat-lying molecules were observed to condense on the surface in two orientations on Ag(111) (Figure 2.14b) [4]. A similar arrangement in the form of long chains is also exhibited by the monolayer of pentacene on Au(111) [29, 30] at room temperature. On Cu(111), the monolayer of pentacene molecules self-assembled into the structure of long chains after short annealing to 400 K and subsequent cooling to room temperature [31]. The adsorption distance of the first molecular layer on Ag(111) was determined to be approximately 0.3 nm, varying slightly with the temperature and surface coverage [5]. The deposition of the second pentacene layer on Ag(111) at room temperature already shows a regular arrangement (Figure 2.14c) [6].

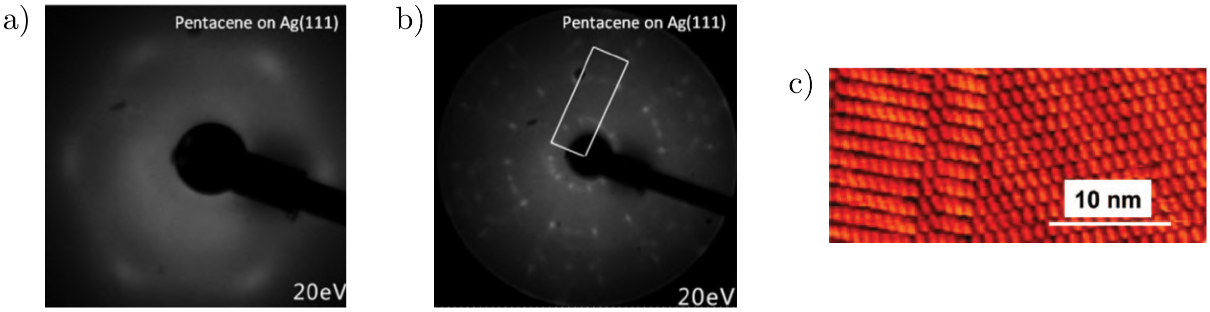

Figure 2.14: (a) LEED pattern of pentacene monolayer on Ag(111) measured at 78 K. A fuzzy diffraction pattern corresponds to a 2D mobile molecular gas. (b) After the deposition of the second monolayer of pentacene, sharp diffraction spots corresponding to a regular arrangement of molecules appeared. Measured at 78 K, taken from [6]. (c) STM image of a regular arrangement of the monolayer of pentacene molecules on Ag(111). Measured at 50 K, taken from [4].

Furthermore, it has been measured that saturation of the change in the work function occurs in the case of pentacene adsorption on the aforementioned metal surfaces when covered by approximately two monolayers [6]. For Ag(111), a change in the work function of nearly 0.6 eV from 4.59 eV for pure Ag(111) to 4.00 eV after the deposition of approximately two monolayers of pentacene was measured [6]. Another source reports a change from 4.50 eV for pure Ag(111) substrate to 3.92 eV after the deposition of over a hundred layers of pentacene [32]. For Au(111), a decrease in the work function after the deposition of two monolayers of pentacene from the initial 5.46 eV to 4.63 eV was measured [6]. Another source reports a decrease from 5.47 eV for pure Au(111) to 4.52 eV after the deposition of over two hundred layers of pentacene [30]. For Cu(111), the change in work function was measured from 4.79 eV to 4.10 eV with coverage of approximately two monolayers [6], or further from 4.92 eV to 4.09 eV after the deposition of over a hundred layers of pentacene [32].

All data regarding the changes in the work function of metals after the deposition of pentacene are presented in Table 2.1. As can be seen, the first two deposited monolayers have the greatest influence on the shift of work function. Additional layers cause only small changes in the vacuum-level shift.

Table 2.1: Work function change after pentacene deposition [6, 30, 32].

Sample	**Amount of pentacene**	**Initial WF**	**Final WF**	**Decrease**
Ag(111)	2 ML	4.59 eV	4.00 eV	0.59 eV
Ag(111)	> 100 ML	4.50 eV	3.92 eV	0.58 eV
Au(111)	2 ML	5.46 eV	4.63 eV	0.83 eV
Au(111)	> 200 ML	5.47 eV	4.52 eV	0.95 eV
Cu(111)	2 ML	4.79 eV	4.10 eV	0.69 eV
Cu(111)	> 100 ML	4.92 eV	4.09 eV	0.83 eV

From the above, it is evident that the pentacene growth at room temperature depends on the particular substrate and its reactivity. While physisorption of pentacene molecules occurs on Au(111), weak chemisorption has been declared for Ag(111) and strong chemisorption for Cu(111) [6]. Although changes in WF can be considered (at least an order of magnitude) comparable, the growth of pentacene differs on each of these surfaces. It will certainly be influenced by our CIL consisting of BTB molecules covering the entire surface of the silver crystal (111).

2.5. Experimental methods

Due to the complicated growth of pentacene even on clean metal substrates, it is convenient that we can use a combination of methods to monitor the growth of the studied system and its subsequent characterization. This chapter briefly describes all the methods used within this thesis.

2.5.1. LEEM device

Low-energy electron microscopy (LEEM) is a method based on the interaction of low-energy electrons (typically 0–50 eV) with the sample surface. One of the main advantages of this technique is the possibility of observing surface processes in real-time. Among other things, it also allows one to quickly switch between different imaging modes, which are described in detail in the following paragraphs. The LEEM technique is only suitable for research of conductive materials, as high voltage has to be applied to the sample. In the case of non-conductive materials, samples are being charged, and the path of incident low-energy electrons is strongly affected, which makes the measurement impossible.

Electrons are emitted from a cold-cathode source producing an electron beam with low energy dispersion, which is essential for imaging. Furthermore, the electrons are accelerated by a voltage of 15 kV relative to the grounded optical system, passing through several magnetic lenses and forming an illumination beam. Subsequently, their trajectory is deflected by 90 ° by a magnetic prism array, whereby electrons are directed perpendicular to the sample surface and focused by the objective lens. The objective lens is grounded as the rest of the optical system and the sample is kept close to the potential of the source. Because of that, electron energy is reduced before they reach the sample surface. De-Broglie wavelength of the low-energy electrons is comparable with the distances between the molecules or atoms of the substrate, so the electrons are diffracted at the surface and accelerated again towards the objective lens. The magnetic prism array again deflects the electrons by 90 °, and after passing through the projection column, they reach the microchannel plate and fluorescent screen that amplifies their signal and convert it to light. The light signal is then detected by a CCD camera.

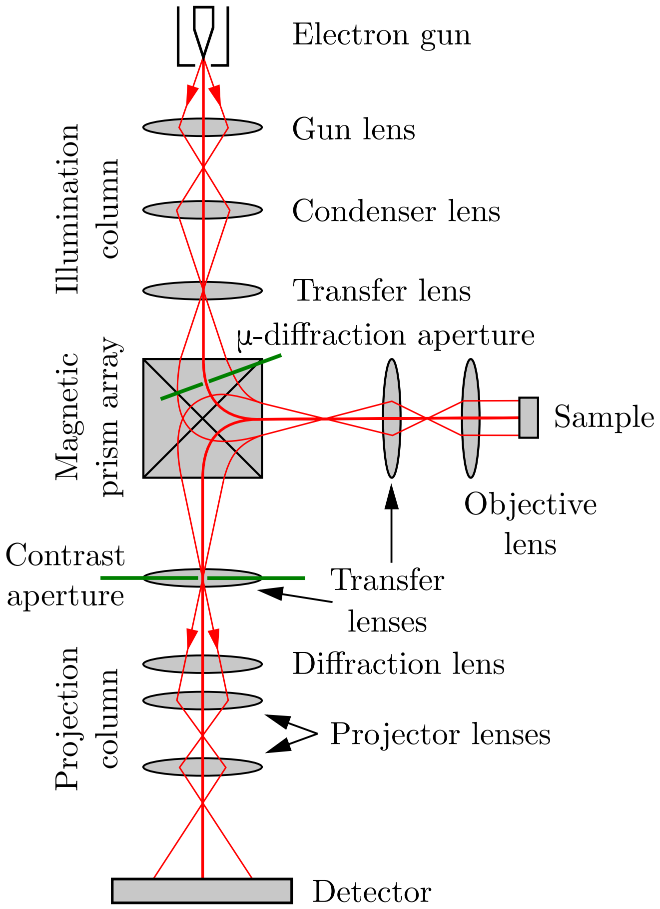

Figure 2.15: Schematic of electron optics in LEEM device. Modified from [7].

2.5.2. Imaging modes in LEEM

We used the LEEM-P90 microscope from SPECS within this thesis. It allows us to measure real space projection and diffraction in several modes. Each of the modes provides different information about the sample surface. Those used within this thesis are described below.

Bright field

Bright-field (BF) mode allows surface mapping with a resolution of up to 10 nm. In this mode, we can image atomic step-edges of the substrate as well as molecular islands on the surface. A contrast aperture is placed in the projection column through which only electrons scattered perpendicularly (so-called $(0,0)$ spot) to the sample surface pass.

Dark field

Conversely, in the dark field (DF) mode, the contrast aperture is set to pass electrons diffracted only in a particular direction. This makes the area where these electrons have been diffracted appear bright, while all other areas appear dark.

BF-IV

The BF-IV (bright field intensity-voltage) curve measurement is based on the measurement of BF as a function of incident beam energy, in our case 0–15 eV, with a step of

0.1 eV. Then, the intensity profile of the pixels corresponding to each prominent spot of the sample area is analyzed. The intensity of the pixels is directly proportional to the number of electrons emitted from a given spot. It will be shown that in the case of pentacene on the BTB monolayer, the number of deposited pentacene layers is equal to the number of local minima in the recorded intensity waveform as a function of electron energy.

Diffraction

In the case of BF and DF imaging, we get a picture of the size and shape of the molecular islands. However, LEEM allows us to measure also in the diffraction mode, which gives us information about the periodicity of molecules on the surface. The prerequisite for getting a clear diffraction pattern is a regularly ordered and clean surface, in our case a mono- or multilayer of adsorbed molecules.

Without inserting a diffraction aperture, the dimensions of the ellipse-shaped beam spot are approximately $15 \times 10\,\mu\mathrm{m}$. Given that the diameter of molecular islands is often in the hundreds of nanometers, the diffraction mode gives us information about all periodic arrangements of molecules from tens of molecular islands in a single image, which includes all the rotational domains. Such a diffraction pattern is usually difficult to analyze. However, one can separate the individual rotational domains using a microdiffraction aperture, which reduces the investigated area to a circle with a diameter of 370 nm (the diameter is given for the fourth diffraction aperture, which we use most often). From the individual rotational domains, one can determine the unit cell of the molecular arrangement. To better understand the relationship between real and reciprocal space, the theory of diffraction is briefly described.

For the case of diffraction on a 2D surface, the law of conservation of momentum applies in the form

$$\mathbf{k}^{\|} - \mathbf{k}_0^{\|} = \mathbf{G}, \tag{2.8}$$

where $\mathbf{k}^{\|}$ is the wave-vector component parallel to the surface of the diffracted electron, $\mathbf{k}_0^{\|}$ is the wave-vector component parallel to the surface of the incident electron, and $\mathbf{G}$ is the reciprocal lattice vector. Both $\mathbf{k}^{\|}$ and $\mathbf{k}_0^{\|}$ vectors must lie on rods perpendicular to the surface where the Ewald sphere intersects them [7, 8]. Reciprocal lattice vector $\mathbf{G}$ is given by

$$\mathbf{G} = h\mathbf{a}_1^* + k\mathbf{a}_2^*, \tag{2.9}$$

where h, k are integers and $\mathbf{a}_1^*$, $\mathbf{a}_2^*$ are the primitive translation vectors of the reciprocal lattice. These reciprocal vectors are associated with the real space vectors via relations

$$\mathbf{a}_1^* = 2\pi \cdot \frac{\mathbf{a}_2 \times \mathbf{n}}{|\mathbf{a}_1 \times \mathbf{a}_2|} \qquad \mathbf{a}_2^* = 2\pi \cdot \frac{\mathbf{n} \times \mathbf{a}_1}{|\mathbf{a}_1 \times \mathbf{a}_2|}, \tag{2.10}$$

where $\mathbf{n}$ is the unit vector of the normal to the surface and $\mathbf{a}_1$ and $\mathbf{a}_2$ are the translation vectors of the real lattice. Based on these formulas, we can create a unit cell of molecules arranged regularly on the surface.

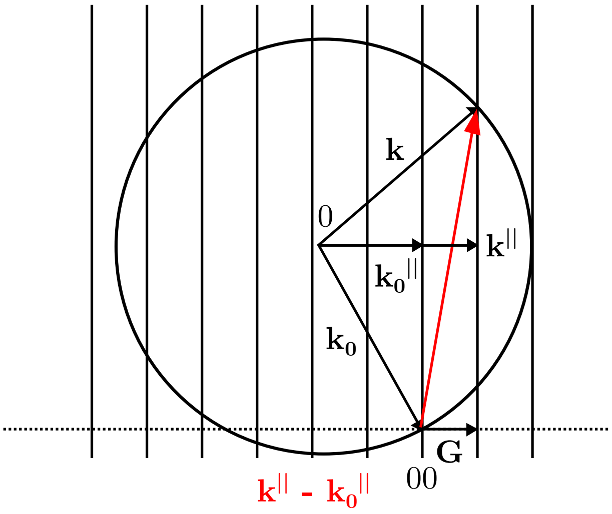

Figure 2.16: Conservation of momentum in diffraction on a 2D lattice. Modified from [7].

PEEM
The image focusing and sample tilt alignment usually starts in the photoemission electron microscopy (PEEM) mode. In this mode, the sample is illuminated by a mercury-based ultraviolet (UV) lamp, which induces the photoemission of electrons from the surface. It is usually used to set the ideal distance of the sample from the objective lens. However, in contrast to low-energy electron imaging, it allows the capture of an area with a diameter of over 200 µm, which is about ten times the diameter that low-energy electron imaging allows. This gives a good picture of, for example, the number of surface defects. As will be shown in the experimental part, this mode has proven to be extremely useful in monitoring the growth of the system we have studied. The LEEM-P90 microscope is also equipped with a He-based UV source with energies 21.2 eV (He I) or 40.8 eV (He II) for energy filtering. This source was not used for measurements in this thesis.

2.5.3. XPS

X-ray photoelectron spectroscopy (XPS) is a commonly used method of detecting the chemical composition of surfaces in surface physics. It is based on the photoelectric effect when high-energy photons eject electrons from the inner orbitals of sample atoms. The process is governed by the following equation

$$E_{\mathrm{kin}} = \hbar\omega - E_{\mathrm{B}} - \phi, \tag{2.11}$$

where E_{kin} is the kinetic energy of the emitted electron, $\hbar$ is the reduced Planck‘s constant, ω is the angular frequency of incident photons, E_{B} is the binding energy of the initial state from which the electron was emitted, and ϕ is the work function of the spectrometer. For an electron to be ejected, the energy of the incident radiation must be higher than the sum of the binding energy and the work function [7].

For the measurement of the chemical composition of the surface to be accurate, we must have a source of ideally monochromatic radiation with high energy. In practice, Mg and Al anodes, which are bombarded with high-energy electrons, are most often used. Due to electron transitions between different orbitals in the bombarded material, highly monochromatic X-rays (with energy 1486.6 eV for Al anode or 1254.6 eV for Mg anode [7]) are emitted together with bremsstrahlung and several satellites. The bremsstrahlung is almost eliminated by the aluminum window through which the photons must pass on their way to the sample. Once the highly monochromatic photons reach the surface, their interaction with the examined sample results in the emission of electrons. Emitted electrons are focused and accelerated by the electron optics into the entrance slit of a hemispherical analyzer, which ensures that only electrons with a certain energy pass through the exit slit onto the detector. In this way, it is possible to scan the entire energy spectrum and thus determine the dependence of the number of emitted electrons as a function of kinetic energy. The binding energy can easily be calculated from the knowledge of the kinetic energy and the initial photon energy. The resulting spectra are dominated by peaks at energies that correspond to the binding energies of electrons in the investigated material. At the same time, they are supplemented by a background due to the inelastic photoelectron scattering and peaks that correspond to Auger transitions.

The chemical composition of the surface is determined from the characteristic peaks of the individual elements in the XPS spectrum. By comparing the peak positions to the tabulated values and by analyzing peak shapes, we are able not only to identify the elements, but also to asses the chemical bonds etc. Only non-scattered and elastically scattered photoelectrons contribute to the peaks. Two different emission angles are commonly used, $0\,^\circ$ (normal) emission and $70\,^\circ$ emission. In $70\,^\circ$ emission mode, only the electrons from a few uppermost monolayers contribute to the peaks, while in the case of normal emission mode, there are more layers from which the electrons contribute to the peaks.

An important factor affecting the measurement is the pass energy E_{pass}, i.e. the energy of the electrons that pass through the hemispherical analyzer. The resolution of the measured spectrum is inversely proportional to E_{pass}, on the other hand, the signal intensity is directly proportional to E_{pass}. For an indicative overview of the chemical composition of the sample, it is advisable to choose a higher E_{pass}. We usually use a pass energy $E_{\mathrm{pass}} = 100\,\mathrm{eV}$ to measure the entire energy spectrum. If we are interested in bonds on the sample surface, we used $E_{\mathrm{pass}} = 20\,\mathrm{eV}$. This allows us to achieve a much better energy resolution required to observe small changes in the position and shape of the peaks.

2.5.4. UPS

Ultraviolet Photoelectron Spectroscopy (UPS) works on the same principle as XPS but uses photons of relatively low energy, so it only maps the valence energy states of the sample. It uses a helium-filled discharge lamp as the radiation source, which, depending on the hydrogen pressure and discharge current, produces highly chromatic ultraviolet light with an energy of 21.2 eV (He I) or 40.8 eV (He II) [7].

From the UPS spectra, one can furthermore read out a lot of information about the valence energy levels of the adsorbed layers, for example, the position of the HOMO. However, we use it only to determine the work function of the sample, and therefore we are only interested in two important values. The first is the position of the Fermi level, from which the emitted electrons have the highest kinetic energy. The second important value is given by secondary electrons, which are considered to be unremovable background in XPS spectra, but here provide valuable information for calculating the sample work function. Since the incident photons have well-defined energy and the sample also has some work function corresponding to the chemical potential of the bulk and surface dipole, electrons with kinetic energy higher than the work function can overcome this energy barrier. For lower kinetic energies this barrier will not be overcome. This kinetic energy is called the secondary-electron cut-off and together with the position of the Fermi-edge can be used to calculate the work function ϕ of the sample from the relation

$$\phi = \hbar\omega - (E_{\mathrm{sec}} - E_{\mathrm{F}}), \tag{2.12}$$

where $\hbar$ is reduced Plank's constant, ω is angular frequency of incoming UV light, E_{sec} is the binding energy of secondary-electron cut-off and E_{F} is the binding energy of Fermi-edge [33].

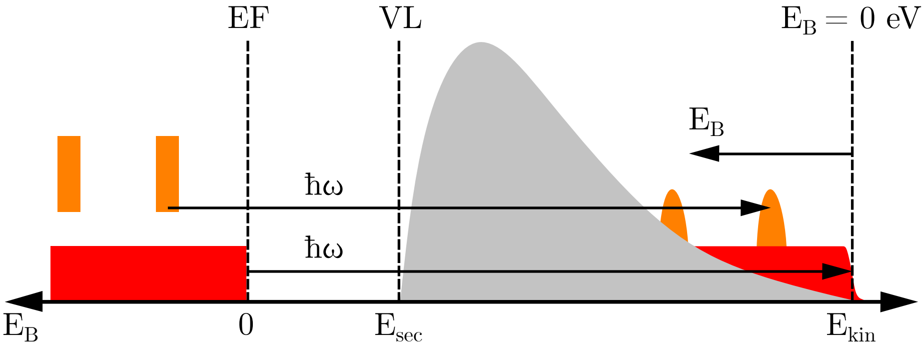

Figure 2.17: Schematic valence energy levels and UPS spectrum of the molecules on a metal substrate. In the UPS spectrum, one can see a gray background corresponding to secondary electrons, orange peaks corresponding to the occupied molecular orbitals and red continuous corresponding to the occupied electronic states of the substrate. Modified from [33].

2.5.5. STM

Scanning tunneling microscopy (STM) is a method based on the quantum tunneling of electrons between two electrodes. One of them is an atomically sharp tip scanning the surface of the sample, the other is the sample itself. Therefore, the STM method is only suitable for research of conductive materials. An atomically sharp tip is most often prepared by electrochemical etching of tungsten wire in hydroxide solutions and then in situ using sputtering, tip indentation into the sample surface, and bias pulses. Scanning of the surface is controlled by a piezoelectric ceramic serving as an electromechanical transducer, which enables the conversion of electrical signals into precise mechanical movement in the order of picometers. The measured quantity is the tunneling current [7, 8].

The tunneling current is exponentially dependent on the distance between the tip and the sample, with the standard distance between the two electrodes during the measurement being less than 1 nm. Because of this, the system must be isolated from ambient vibrations. This can be achieved by magnetic levitation, spring suspension, and other methods. The system must also include a mechanism for the macroscopic approach of the tip to the sample so that the automatic mechanism for the microscopic approach can subsequently be started [7, 8].

The exponential dependence of the tunneling current on the distance between the electrodes together with piezoelectric mechanics and feedback electronics allow us to obtain images of the surface with atomic resolution. However, it should be kept in mind that the tunneling current depends on the local density of states. For this reason, maxima in STM images can correspond to both topographic and electronic protrusions.

Two measurement modes are most often used to measure the surface of the sample. The first of these is the constant current mode when the position of the tip in the z axis is changed so that a constant tunneling current is maintained. Therefore, the result of the measurement is a map of the dependence of the z position on the position in the x and y axes. This mode makes it possible to examine surfaces with high defects, atomic steps, and so on [7].

The second mode is the constant height mode, when a constant position of the tip in the z axis is maintained, resulting in a map of the dependence of the tunneling current on the position in the x and y axes. Scanning at a constant height allows us to achieve better resolution and contrast of the resulting image. However, the disadvantage is that it only allows us to scan parts of the surface that have already been partially mapped and we know that there are no protrusions, as contact of the tip with the surface usually causes the loss of the atomically sharp tip. Its restoration is usually a very time-consuming process [7].

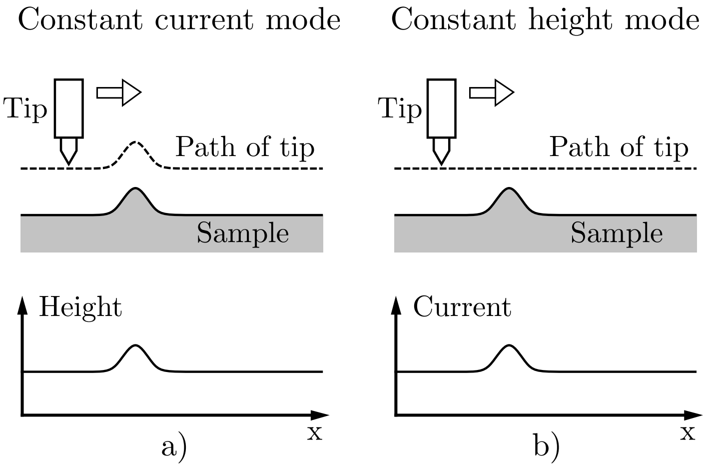

Figure 2.18: Schematic of two measurement modes used in STM. Modified from [7].

3. Experimental part

This chapter contains a description of the experimental procedures used within this thesis and a discussion of the results. The experimental part of this thesis is primarily focused on utilizing the fully deprotonated BTB molecular layer on Ag(111) as a substrate for the subsequent growth of pentacene layers. A detailed description of the individual phases and phase transformations of BTB molecules from their protonated state, as well as the electronic properties of individual phases, will be described later in a dedicated publication of our research group.

As a metal substrate, we used Ag crystal with (111) surface termination, which is often used both for BTB growth studies and for investigating the electronic properties of pentacene layers. The cylinder-shaped crystal with a base diameter of 10 mm and a height of 3 mm was supplied by SPL. To allow sample handling in the UHV environment, we placed the substrate in a special sample holder. BTB molecules of 98 % purity and pentacene molecules of 99 % purity were supplied by Sigma-Aldrich.

All experimental work, including the substrate preparation and the deposition of the molecules, was carried out on the UHV cluster at CEITEC Nano Research Infrastructure. The UHV cluster is composed of nine chambers connected by a linear transfer system (LTS). The schematic of the cluster and the importance of each chamber are summarized in Figure 3.1. The base pressure of each chamber including the LTS is $2 \cdot 10^{-10}$ mbar.

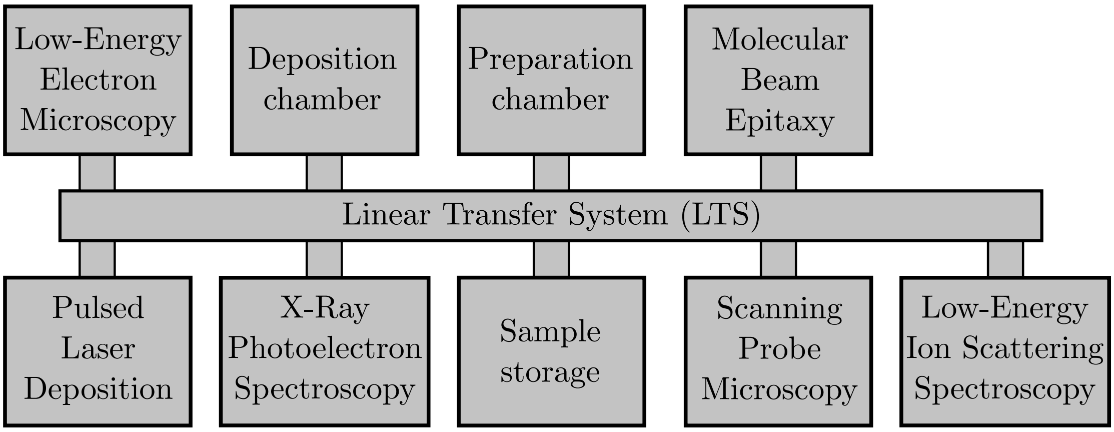

Figure 3.1: Schematics of the UHV cluster at CEITEC Nano.

3.1. Parameters of LEEM images

The growth of the investigated system was characterized by the combination of the PEEM and BF measurements. To differentiate between PEEM and BF images easily, PEEM images are cropped to a square shape, while images measured by low-energy electrons are cropped to a circle.

For BF and DF images, the energy of electrons used for imaging is written for each image. This is especially important because contrast inversion can (and does) occur at various energies. Most of these images were also measured with the fourth contrast aperture inserted.

Also, we measured diffraction patterns using LEEM (in diffraction mode). We usually used electrons with an energy of 10 eV to monitor the phase and transformation of CIL, because it provides the highest intensity of BTB diffraction spots corresponding to the reciprocal cell. For the same reason, electrons with an energy of 13 eV were usually used to characterize the pentacene layer. To reduce the noise in diffraction patterns, it was preferable to insert the first microdiffraction aperture, which limits the size of the electron beam to a diameter of 3.7 μm. This area still enables to measure multiple rotational domains simultaneously. For microdiffraction measurements, we inserted the fourth microdiffraction aperture, which has a diameter of 370 nm and allowed us to measure single rotational domains.

3.2. Substrate preparation

After inserting any single crystal sample into the UHV, or if the sample has already been placed in the UHV but has not been used for a long time, it is first necessary to start with degassing. This is achieved by very slow heating in the preparation chamber to the target temperature at which the crystal will subsequently be cleaned. A long, low-temperature degassing is necessary to allow the gradual desorption of water and other molecules adsorbed on the crystal and the sample holder surface under atmospheric conditions. A rapid increase in temperature would result in a sharp increase in chamber pressure, which we want to avoid in order to keep the chamber clean for the following experiments and because of the potential damage to the vacuum pumps.

Subsequently, we used sputtering-annealing cycles for the crystal cleaning. During the first cleaning, it is necessary to perform several of these cycles to remove most of the impurities. However, if there are only the molecules at the surface deposited from the recently performed experiment, it is usually enough to perform two of these cycles.

Cleaning always begins with rapid heating of the sample to a temperature of approximately 350 °C (the minimum temperature that can be determined by the pyrometer we use) to evaporate all the organics from the previous experiment. During the substrate sputtering, Ar cations are accelerated towards the surface in the range of 1.2–2.1 keV. We used a $1 \cdot 10^{-5}$ mbar partial pressure of Ar^{+}. In the first cycle, we often sputtered at an angle of 20 ° relative to the surface normal, by which we wanted to achieve higher sputtering efficiency. During the second sputtering cycle, we sputtered perpendicular to the surface plane. Sputtering took 10–15 minutes, which was always enough to remove most of the impurities.

Subsequently, the surface structure was restored by sample annealing. Heating of the sample usually took 5–7 minutes, with the target temperature being 510–520 °C. Then, the sample was kept at this temperature for two minutes. Cooling down the sample from the target temperature to a temperature of approximately 350 °C usually took 7–10 min. The heating filament was then switched off. The next sputtering-annealing cycle was started immediately, without waiting for the sample to cool down. The cooling rate was optimized for the largest size of atomic terraces. The cleaned Ag(111) surface can be seen in Figure 3.2a.

After cleaning the sample and cooling it to room temperature, we proceeded to the deposition of BTB molecules in the deposition chamber.

3.3. Fabrication of CIL

The deposition of BTB molecules on a clean Ag(111) substrate was carried out in the deposition chamber using the effusion cell described in Chapter 2.1. The only difference was that the crucible containing the molecules was not heated by the filament but by preheated oil. The advantage of this system is mainly high temperature stability during the deposition. However, due to the high deposition temperature we used, the oil gradually degraded and lost its ability to heat the molecules. Therefore, we had to gradually increase the deposition temperature of the oil from the initial 250 °C to 265 °C, while also increasing the deposition time. In the first experiments, it was sufficient to deposit for about 120 minutes, while in the last experiments, we had to deposit for more than 150 minutes.

BF images of the Ag(111) surface after the deposition of approximately 1 ML of BTB molecules can be seen in Figures 3.2b and 3.2c. Dark lines represent atomic step-edges. Although determining the submonolayer coverage of BTB molecules was relatively easy, after deposition of approximately 1 ML, islands of the second layer begin to form without the first layer being filled. Therefore, it was difficult to determine whether less than a monolayer or more than a monolayer of molecules was deposited.

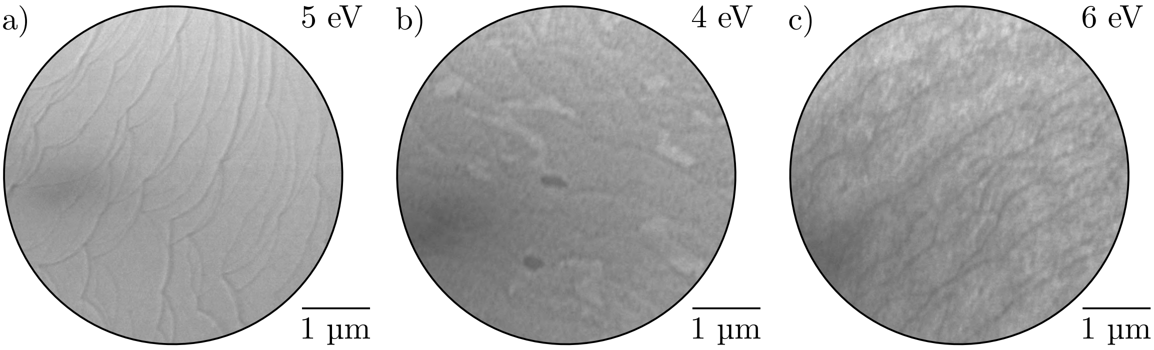

Figure 3.2: (a) BF image of the cleaned Ag(111) surface. (b) BF image of the as-deposited BTB on Ag(111) after deposition of approximately 1 ML at 4 eV and (c) 6 eV. The dark lines correspond to atomic step-edges. It is difficult to determine from the images whether the individual regions correspond to the first layer, the second layer, or the molecular gas.

The diffraction pattern of as-deposited BTB molecules can be seen in Figure 3.3a. Fuzzy diffraction spots correspond to an imperfect arrangement of molecules on the surface. XPS measurements revealed a sharp C1s peak and a broad O1s. The O1s peak corresponds to fully protonated molecules as it consists of hydroxyl and carbonyl oxygen contributions. A similar peak shape was measured for the fully protonated phase of BDA molecules, which also contain -COOH groups [19, 21].

Because of the imperfect arrangement of as-deposited molecules, we decided to thermally transform the deposited layer. The gradual change in the diffraction pattern can be seen in Figures 3.3a–d. With the increasing temperature the diffraction pattern changed and spots became sharper, which indicates a better arrangement of molecules. The rearrangement of molecules stopped after reaching a temperature of approximately 170 °C (according to the low-temperature pyrometer with emissivity 0.1, heating filament current was set to 1.8 A for 10 minutes without applied voltage), resulting in a molecular arrangement to which corresponds a very sharp diffraction pattern (Figure 3.3d). During subsequent annealing at higher temperatures, no further rearrangement occurred. The sharp diffraction pattern was then measured with the first microdiffraction aperture inserted (Figure 3.3e and 3.3f).

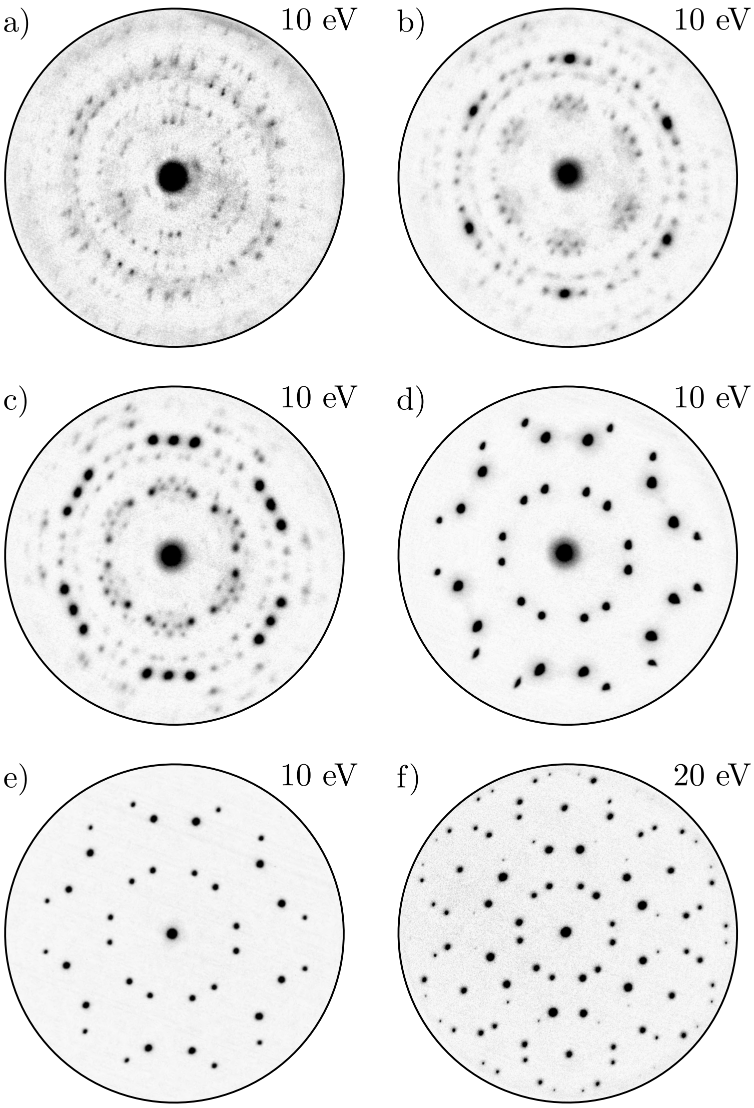

Figure 3.3: Evolution of the diffraction pattern of the BTB layer on Ag(111) substrate during its annealing. (a) Diffraction pattern of the as-deposited molecular layer. (b, c) Approximately after 5 minutes of annealing with a heating current set to 1.8 A, the molecules started to deprotonate, which induced their phase transformation. (d) A sharp diffraction pattern corresponding to the final molecular arrangement achieved after approximately 10 minutes of annealing when the temperature of approx. 170 °C was reached. (e) Diffraction pattern of the resulting arrangement measured using the first microdiffraction aperture at an electron energy of 10 eV and (f) 20 eV.

It is important to note here that the diffraction pattern of thermally transformed molecules combines two rotational domains of the molecules. The diffraction spots corresponding to each rotational domain are shown in Figure 3.23.

Using room temperature (RT) STM, we measured that the resulting diffraction pattern corresponds to the close-packed 2D monolayer as reported by Ruben et al. [23]. Figure

3.4 shows one of the two rotational domains of the molecules. In the second rotational domain, molecules are rotated by 60 °.

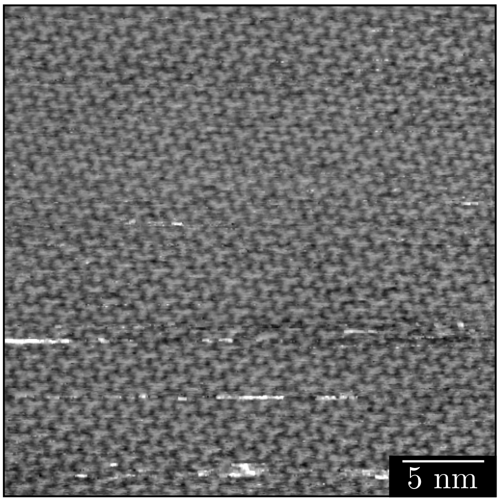

Figure 3.4: STM image of the one of two rotational domains of close-packed 2D monolayer formed by BTB molecules. Measured at RT, $U_S = 0.2\,V$, $I = 50\,pA$.

XPS measurement of the close-packed 2D monolayer (Figure 3.5) shows the sharp carbon and oxygen peaks, which suggests that the close-packed arrangement consists only of fully deprotonated molecules [19]. In this case, there is a contradiction with the model published by Ruben et al. [23] which proposed only two-thirds deprotonation of the molecules forming the close-packed structure.

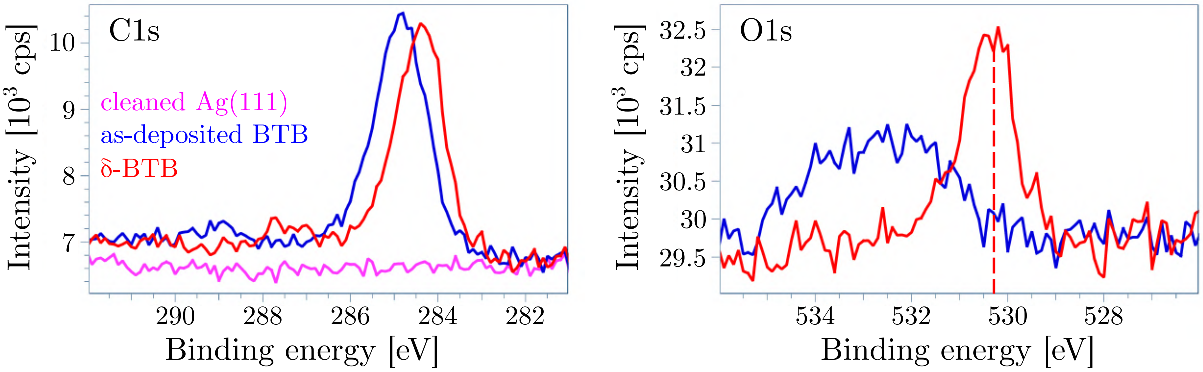

Figure 3.5: XPS spectra of carbon and oxygen peak after cleaning the Ag(111) crystal, deposition of approximately 1 ML of BTB molecules, and their phase transformation to δ-phase. No C1s peak was observed after two sputtering-annealing cycles, indicating that the surface was cleaned properly. A broad O1s was measured after the deposition of the BTB molecules. The shape of the peak corresponds to the fully protonated molecules as it consists of hydroxyl and carbonyl oxygen contributions. After the transformation to δ-phase, a sharp O1s peak was measured, indicating that the surface is covered only by fully deprotonated BTB molecules. Measured in normal emission mode at RT with Mg X-ray source operating at power $P = 300\,W$.

Since the resulting arrangement after annealing at 170 ° C consists only of fully deprotonated molecules, we denote this molecular phase as δ-phase, as in the case of the fully deprotonated phase of BDA molecules [19].

Figure 3.6a shows the BF image of the surface after the phase transformation of BTB molecules into the δ-phase, measured at 5 eV. The atomic step-edges of the Ag(111) surface are clearly visible as thicker dark lines (highlighted by a yellow arrow). Moreover, measurement at this energy allows us to distinguish individual molecular domains by visualization of domain boundaries (thinner lines on atomic terraces of the substrate, highlighted by a green arrow). Measurement at 16 eV then allows distinguishing regions belonging to the individual rotational domains of δ-BTB molecules (highlighted by a cyan and and orange arrow in Figure 3.6b).

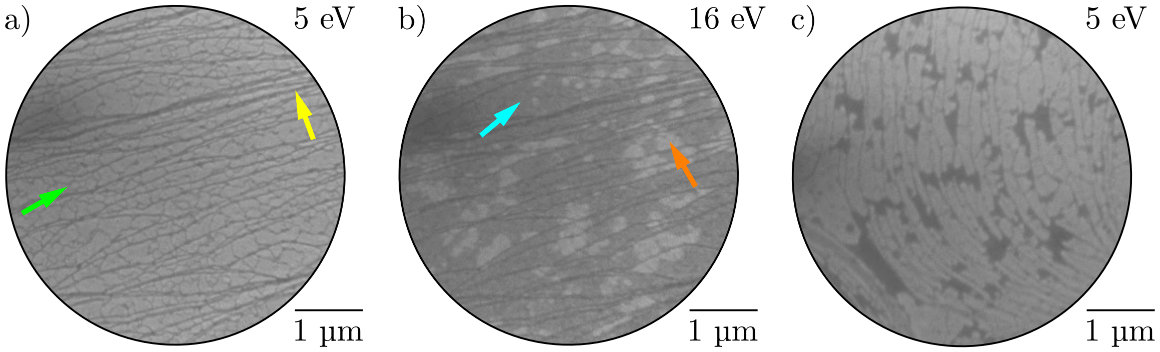

Figure 3.6: BF images of δ-BTB monolayer. (a) As can be seen, atomic step-edges (highlighted by a yellow arrow) of the Ag(111) surface and δ-BTB domain boundaries (highlighted by with green arrow) can be visualized at 5 eV. (b) At 16 eV, two rotational domains are well resolved due to the two distinct levels of the reflected intensity (highlighted by a cyan arrow and an orange arrow). (c) BF image of the submonolayer of δ-BTB molecules on Ag(111). The dark areas are holes in the (bright) layer of molecules. To obtain a full layer of δ-BTB molecules, more than 1 ML of BTB must be deposited, since the δ-phase corresponds to a higher density of molecules than the as-deposited phase [23].

We always aimed to deposit more than 1 ML of molecules, because the subsequent thermal transformation of molecules causes their rearrangement into the more compact δ-phase, which reduces the molecular coverage. If only exactly one monolayer was deposited, or slightly less than one monolayer, the non-compact layer was formed, as shown in Figure 3.6c, where bright regions represent the molecular layer. Additional deposition of BTB molecules on a such incomplete layer and subsequent heating of the sample results in the full layer of δ-BTB (assuming that enough molecules have been deposited).

Due to the high homogeneity of the δ-phase, we decided to use it as a CIL for subsequent pentacene deposition.

3.4. Pentacene growth

The homogeneous and compact δ-BTB layer was subsequently used as a substrate for the deposition of pentacene molecules. In this case, the pentacene molecules were deposited directly in the LEEM from the effusion cell heated by a tungsten wire. After in-situ real-time deposition experiments, we calibrated a deposition temperature to 170 °C, which corresponds to a heating current of 1.26 A. The temperature stability during the measurements was ± 2 °C.

In total, we performed ten different in-situ depositions of pentacene molecules. In all cases where we used the same Ag(111) crystal and managed to prepare a homogeneous CIL, the growth proceeded very similarly. For the sake of clarity, we have divided the pentacene growth into four stages.

3.4.1. The first stage of pentacene growth

No significant changes were observed during the first 30 minutes of the deposition. Diffraction remained unchanged, only a slight blurring of the diffraction spots corresponding to δ-BTB was observed. This suggests that the pentacene molecules are accumulated on the surface in the form of a 2D molecular gas.

After 30 to 40 minutes, large compact molecular islands (highlighted by a yellow arrow) started to nucleate across the surface of the sample as can be seen in the PEEM image in Figure 3.7a. Within moments, approximately 10 % of the surface was covered by these large islands, often up to 200 µm in diameter. The area between these islands is covered by molecular gas. Due to their size, it was not possible to determine the surface coverage of these islands from individual BF images. However, it could be determined from several PEEM measurements, which allow capturing a surface area with a diameter of up to 250 µm.

This type of growth can be explained by the high critical size of the nuclei that needs to be exceeded for the formation of a stable island. In such a case, the surface must be highly supersaturated with molecules to allow the nucleation of islands and their subsequent rapid growth.

It is also important to mention that the nucleation and the growth of large pentacene islands were never observed in PEEM mode when the sample was illuminated with UV light. If the UV light was switched off and then switched on again after a few minutes, the surface was covered by these compact islands. Therefore, we conclude that UV light prevents the nucleation of the pentacene islands. The growth of pentacene islands in PEEM mode was typically monitored by opening the shutter shielding the UV light every 10 minutes and rapidly scanning over the sample surface to check the growth stage. The shutter was then closed to minimize the negative effect of the UV light on the growth and the surface was checked again after another 10 minutes.

BF image in Figure 3.7b measured on pentacene island clearly shows that these islands are not compact in this growth stage. Dark areas (highlighted by a white arrow) represent the δ-BTB substrate (or a pentacene molecular gas), while brighter areas are the pentacene layer. Moreover, pentacene molecular islands show two distinct levels of intensity (highlighted by a blue arrow and a green arrow), which we attribute to the two rotational domains of underlying δ-BTB molecules. This interpretation is supported by the BF-IV measurements, which we describe in Chapter 3.5.1. Figure 3.7c shows the diffraction pattern of the pentacene layer, which will also be analyzed in more detail in Chapter 3.5.3. The δ-BTB diffraction spots are highlighted by red circles. Images 3.7d–f show the edge of the pentacene island measured at different energies. The electron reflectivity in BF images is strongly energy-dependent.

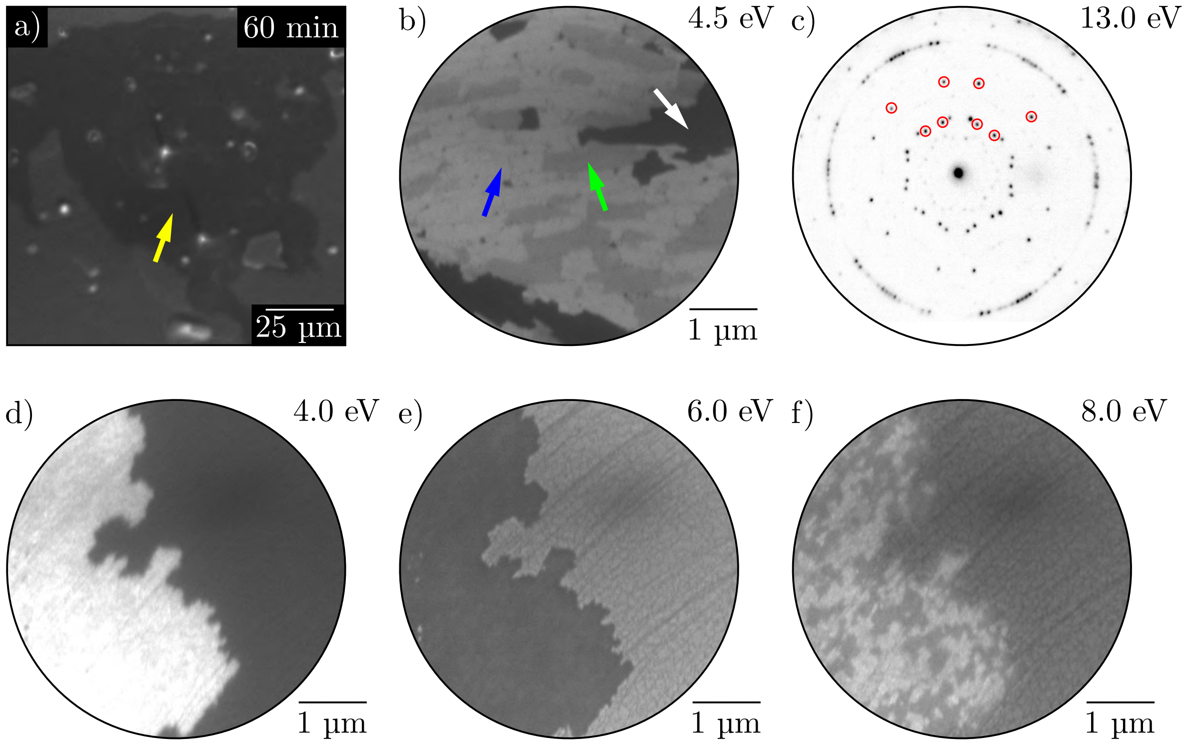

Figure 3.7: (a) PEEM image of a large pentacene island (dark areas in the image, highlighted by a yellow arrow) formed in the first growth stage. (b) BF image of a pentacene island. At this energy, two distinct levels of intensity (highlighted by a blue arrow and a green arrow) correspond to the pentacene layer on top of the two rotational domains of δ-BTB and dark areas correspond to holes in the pentacene island. (c) Diffraction pattern of the grown pentacene islands. The marked spots (and other spots rotated by 120 ° to either side) correspond to the δ-BTB layer. We deal with a detailed analysis of the diffraction pattern in Chapter 3.5.3. (d)–(f) BF images of the edge of the pentacene island measured at different energies. The pentacene island is in the left part of the images. As can be seen, the mutual contrast between the underlying δ-BTB layer and the pentacene island changes significantly. This will be further explored in Chapter 3.5.1.

The subsequent growth of molecular islands proceeded in unpredictable directions. Figure 3.8a shows one of the molecular islands shortly after nucleation (40 minutes after the start of the pentacene deposition) and Figure 3.8b shows the same region after another 30 minutes of the deposition. Between image acquisitions, the UV light was shielded by a shutter. As can be seen, molecular island growth occurred in only one particular area (marked in green in Figure 3.8b). There was no growth in the other directions.

We tried several times to capture the initial nucleation of molecular islands in BF mode, but were never successful. Considering the size of the electron beam (approx. $15 \times 10\,\mu\mathrm{m}$) and the density of islands, monitoring the nucleation is almost impossible. After the initial nucleation, we once encountered a region in the BF mode from which a pentacene island was growing. However, the growth stopped very quickly after electron illumination, indicating a negative impact of the electron beam on the growth of the pentacene islands.

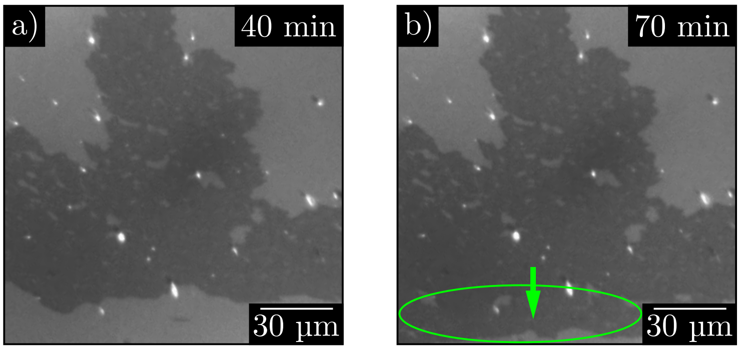

Figure 3.8: PEEM images showing the first stage of pentacene growth. Large, compact islands (dark areas in the image) do not grow uniformly, but in unpredictable directions and shapes. Image (a) was taken after 40 minutes of deposition and image (b) after another 30 minutes later. In between the images, the shutter of the UV lamp was closed.

3.4.2. The second stage of pentacene growth

In the second growth stage, which generally lasted from the initial nucleation of large molecular islands to a total of 120 minutes of deposition, the dendritic growth of molecular islands was observed. The PEEM measurement of this growth is summarized in Figure 3.9. In this case, the sample was illuminated with UV light between Figures 3.9a–c acquisition. Dendrites were always connected to the initial compact islands at some point.

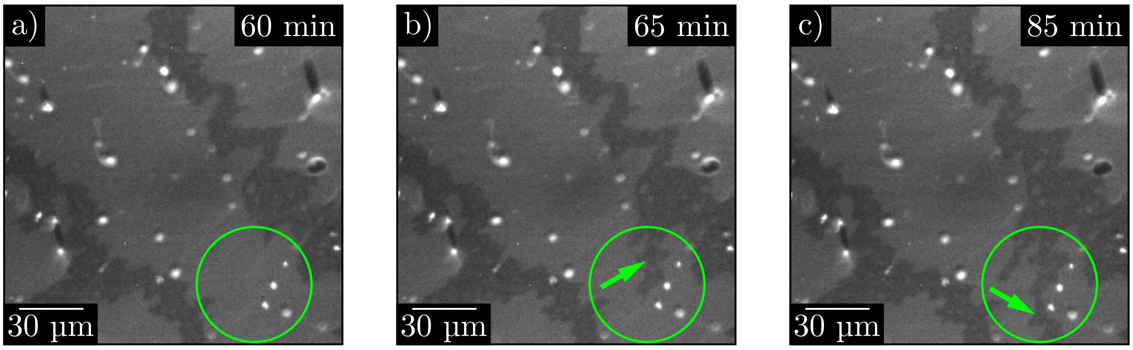

Figure 3.9: PEEM images showing the second stage of pentacene growth in time. After the large compact islands have been formed over about 10 % of the surface, the growth of dendrites (highlighted by green arrows and circles) was observed. The sample was illuminated with UV light all the time between image acquisition.

3.4.3. The third stage of pentacene growth

In the third stage of pentacene growth, the nucleation and the growth of the second layer of pentacene islands occur. This growth stage usually starts after approximately two hours of the deposition. The nucleation of second layer islands and their subsequent growth was clearly visible both in PEEM (highlighted by cyan arrows in Figures 3.10a and 3.10b) and BF mode (marked with red arrows in Figure 3.11). In PEEM, the second layer appears as darker areas growing on top of the dark areas of the first layer, as can be seen in Figures 3.10a and 3.10b.

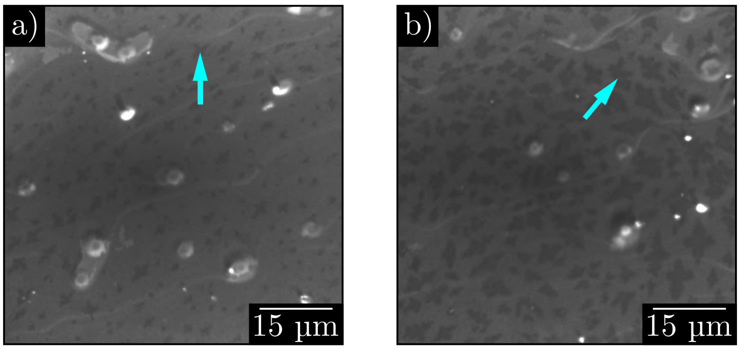

Figure 3.10: PEEM images showing the third stage of pentacene growth. The darkest islands (marked with cyan arrows) correspond to the second pentacene layer, which will be verified later in Chapter 3.5.1.

BF measurement in Figure 3.11 allows the description of the third pentacene growth stage in more detail. The brightest area in the red circle in Figure 3.11a shows the pre-existing island of the second layer (which was already present in the imaged region before the low-energy electron illumination) that grows during the measurement. At the same time, the first pentacene layer also grows in available space, as shown in green circles and marked with green arrows in Figure 3.11b. Moreover, the nucleation of another second layer islands and their subsequent growth occurs (marked with blue circles in Figure 3.11c).

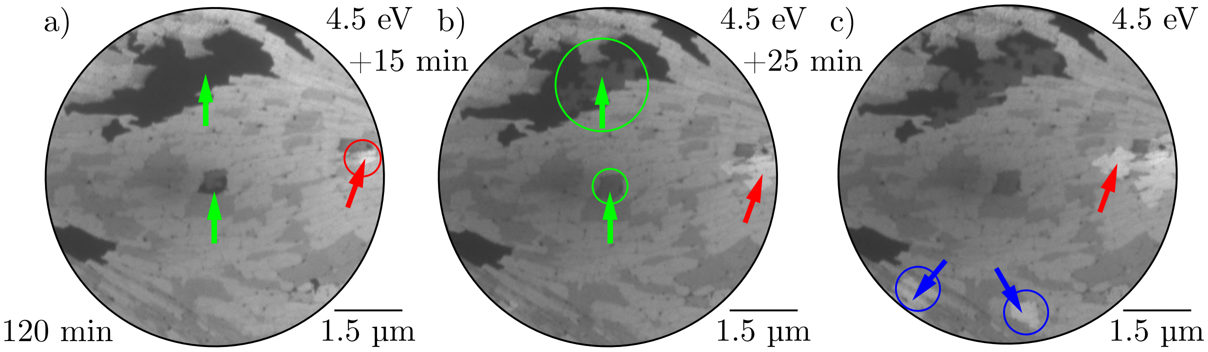

Figure 3.11: BF images showing the third stage of pentacene growth. Dark areas (marked with green arrows) correspond to the holes in the first pentacene layer and two distinct grey areas correspond to the monolayer of pentacene, which grows on top of the two rotational domains of δ-BTB molecules. (a) The bright area enclosed in a red circle corresponds to the second pentacene layer. (b) Green circles mark the areas, where the holes in the first pentacene layer are gradually filled. The image was taken 15 minutes after the first one. (c) Blue circles mark the areas where nucleation of the second layer islands occurs. The area was illuminated with low-energy electrons the entire time between the images acquisition.

During the measurement of Figure 3.11, the surface area was continuously irradiated by the electron beam. No negative effect of low-energy electrons or UV light on the growth of the second pentacene layer was observed. In general, the more compact the first pentacene layer was (or the fewer holes there were in it), the earlier the second layer nucleation started. Supporting data for the interpretation of the measured results are presented in Chapter 3.5.1.

3.4.4. The fourth stage of pentacene growth

In the last growth stage, which typically started after three hours of the pentacene deposition, the growth mode of the pentacene layer dramatically changed. New needle-like structures started to grow between molecular islands (marked with a yellow arrow in Figure 3.12a) and also directly from the edges of molecular islands (marked with a cyan arrow in Figure 3.12b and green arrows in 3.12c). The same area as in 3.12a was also measured in BF mode in Figure 3.12b, which shows the initial molecular island (marked with an orange arrow) from the first and second stages and also the needle-like structure (marked with a cyan arrow) in more detail.

Once the fourth growth stage started, no further growth of the first pentacene layer was observed. There was only further growth of needle-like structures, slow growth of second layer islands and filling in the last holes in the compact islands. Because we are mainly focused on the growth (and subsequent characterization) of uniform layer(s) that almost did not extend since the beginning of the fourth growth stage (except for the slow growth of the second layer islands), we decided to always stop the deposition at this point.

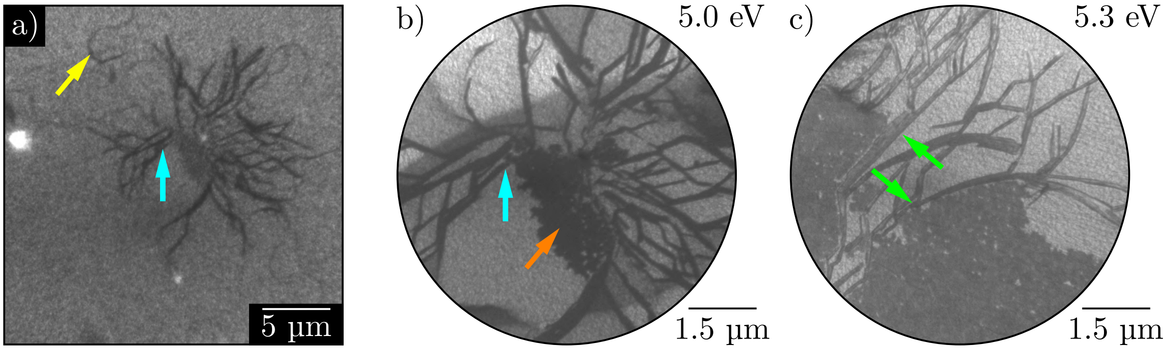

Figure 3.12: (a) PEEM image showing the fourth stage of pentacene growth, when needle-like structures started to grow (approximatelly after 3 hours of the deposition). Whenever these objects appeared on the surface, the first pentacene layer stopped growing. (b) BF image of the same area as in (a) showing the initial molecular island (marked with an orange arrow) and also the needle-like structure (marked with a cyan arrow) in more detail. (c) BF image of the needle-like structure (marked with green arrows) which started to grow from the edge of the pentacene island.

3.4.5. Achieving maximum coverage

We can say that the maximum possible coverage of the 2D ordered pentacene structures was achieved once the fourth growth stage started. This coverage has been estimated from many PEEM images to be approximately 20 %.

Thus, after the deposition was finished, the surface was covered with various formations. In the first place, there were compact molecular islands, partially covered by a second layer of molecules (Figure 3.13a). There were also dendrites of the first layer. Depending on their compactness, some dendrites were partially covered by a second layer of pentacene molecules (Figure 3.13b). Lastly, the needle-like structures can be found on the surface. However, it should be mentioned again that approximately 80 % of the surface is covered only by the 2D molecular gas. The density of the molecular gas cannot be accurately estimated unless we have a comparison with a full layer of pentacene molecules where the molecular gas is no longer present.

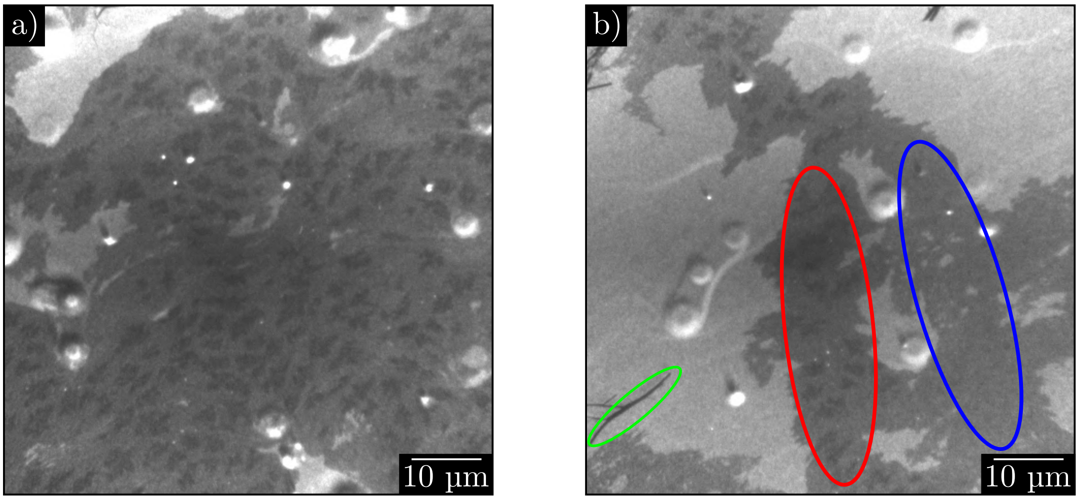

Figure 3.13: PEEM images showing the different structures on the surface after achieving maximum coverage of about 20 %. (a) A compact pentacene island, on which the second layer of pentacene started to grow, forming smaller islands. (b) Between compact islands, there were dendritic structures, on which may (marked in red) or may not (marked in blue) grew the second layer islands. A needle-like structure is marked in green.

3.4.6. Annealing of the resulting structures

The resulting structure was annealed after the deposition was completed, in an attempt to desorb only the molecules forming the needle-like structures, while preserving the existing molecular islands. However, as can be seen in Figure 3.14, the molecules from the islands and the needle-like structures began to desorb simultaneously (at approximately 80 °C). Thus, it was not possible to get rid of the needle-like structures in this way and then continue with deposition.

The XPS spectrum after the sample annealing showed that a significant amount of pentacene remains on the surface. In contrast to BTB, pentacene molecules consist only of carbon and hydrogen atoms, but not oxygen. If pentacene is present on the surface (even in the form of 2D molecular gas), the oxygen peak should decrease and the carbon peak increase compared to the measurement after the δ-BTB monolayer was formed, which can be exactly seen in Figure 3.15. The red spectrum corresponds to the state after the formation of a complete δ-BTB monolayer. The green spectrum was measured after the fourth stage of pentacene growth and subsequent annealing at approximately 80 °C. The annealing was terminated when the last parts of the molecular islands and needle-like structures disappeared.

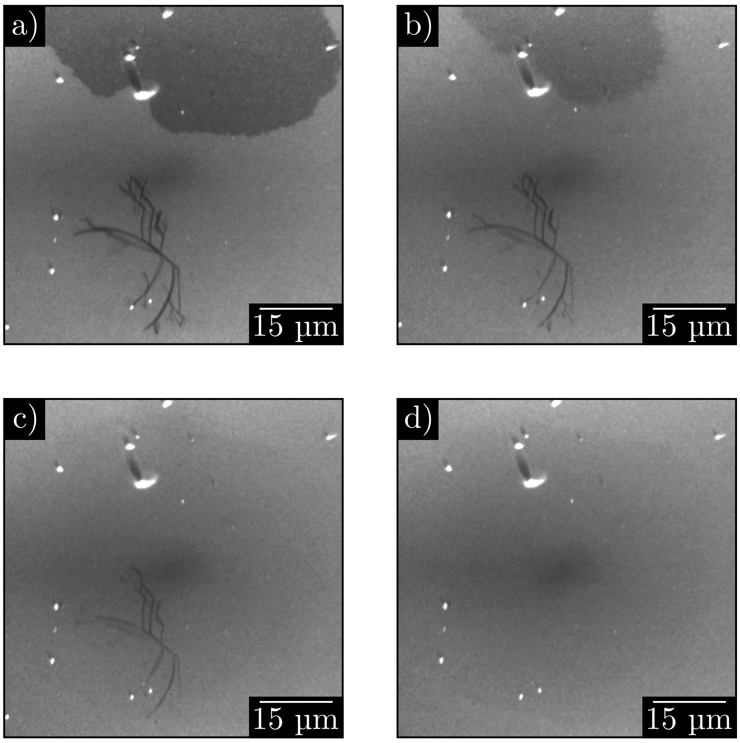

Figure 3.14: PEEM images showing annealing of the molecular layer after the fourth growth stage. As can be seen in (b) and (c), the molecules started to desorb from both island and needle-like structure at the same time at approximately 80 °C. Therefore, it was not possible to remove only the needle-like structures and continue with the deposition.

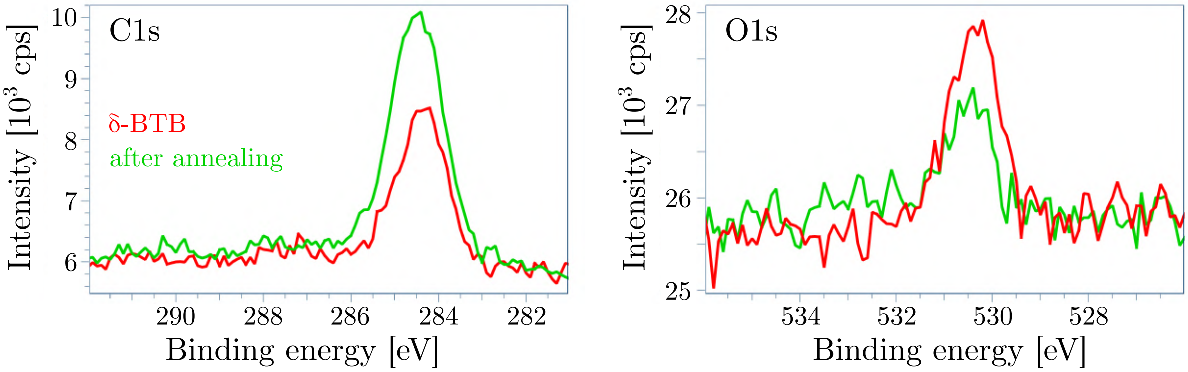

Figure 3.15: XPS spectra of δ-BTB monolayer and after annealing of the pentacene islands and needle-like structures. The height of both peaks indicates that a large amount of pentacene remained on the surface after the molecular islands and needle-like structures disappeared. Measured in normal emission mode at RT with Mg X-ray source operating at power P = 300 W.

The preservation of the δ-BTB monolayer after annealing is confirmed by the unchanged diffraction pattern (Figure 3.16a) and BF images (Figure 3.16b and 3.16c).

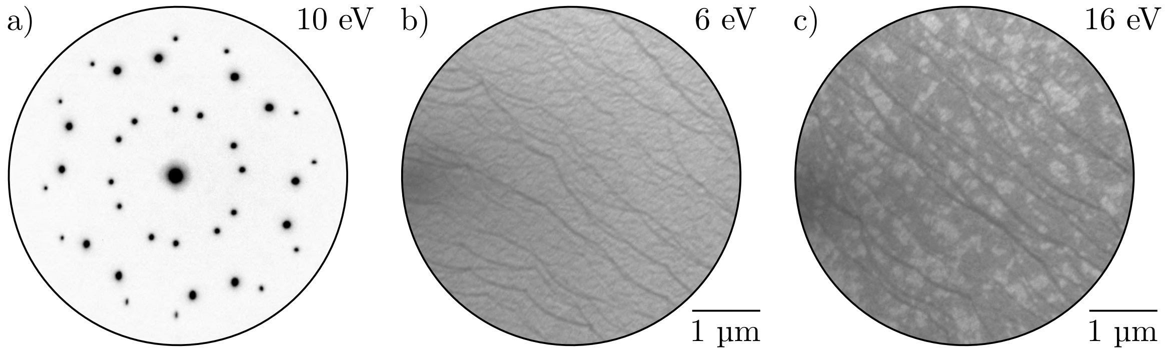

Figure 3.16: (a) Diffraction pattern of the δ-BTB monolayer after pentacene deposition and subsequent annealing. (b, c) BF images of the δ-BTB monolayer after pentacene deposition and subsequent annealing. Since we do not observe any changes in the images, we assume that the δ-BTB monolayer remained unchanged during the deposition of pentacene and subsequent annealing.

3.5. Characterization of pentacene layers

3.5.1. BF image intensity interpretation

The interpretation of our results so far was based mainly on the contrast differences in LEEM BF ad PEEM measurements. We could see that in the PEEM mode, huge pentacene islands and dendritic structures after the first and second growth stages are visible, which correspond to the dark areas on a bright substrate covered with CIL. A second pentacene layer appears even darker in the PEEM mode. This layer grows in the form of smaller islands distributed over the surface of the compact islands of the first pentacene layer.

In BF mode, high contrast between the pentacene layer and the underlying δ-BTB layer was obtained at electron energy 4.5 eV. At this energy, the pentacene bilayer gives the maximum reflected intensity, the single layer gives lower reflected intensity, and the underlying δ-BTB layer gives the lowest reflected intensity. Moreover, two slightly different intensities were observed for pentacene single-layer islands. Since the mutual contrast of the individual layers varies with the electron energy, we decided to plot the reflected intensity dependence for each layer into IV curves.

The area in Figure 3.17a was measured on the center of the pentacene island, whereas the area in Figure 3.17c was on its edge, both in BF mode. Both figures show regions with single and double pentacene layers, which were recorded as a function of incident electron energy from 0 up to 15 eV with the step of 0.1 eV. The colored squares inside BF images show areas from which we summed the intensity and plotted it as a function of energy (Figure 3.17b and 3.17d). Dimension of squares was always 20×20 px, which corresponds to an area of approx. 150×150 nm. The colors of IV curves in Figure 3.17b and 3.17d correspond to the colors of squares in Figure 3.17a and 3.17c (except for the black curve, which comes from the white square for better visibility).

As can be seen, the curves corresponding to the brightest regions (darkest in PEEM), which we have so far interpreted as pentacene bilayers, have two local minima in the range of 5–7 eV. The curves corresponding to the two distinct grey regions, which we have so far interpreted as a pentacene monolayer growing on the two different rotational domains of the underlying BTB molecules, have only one local minimum over the same energy range. Finally, the curves corresponding to the dark regions, which we have so far interpreted as the δ-BTB layer without pentacene island, have no local minimum on the given energy interval. The results are identical for both regions. The same dependence was measured in the case of a monolayer, bilayer and trilayer of graphene on SiC, where the number of local minima of IV curves in the energy range of 0–7 eV also coincided with the number of graphene layers [34].

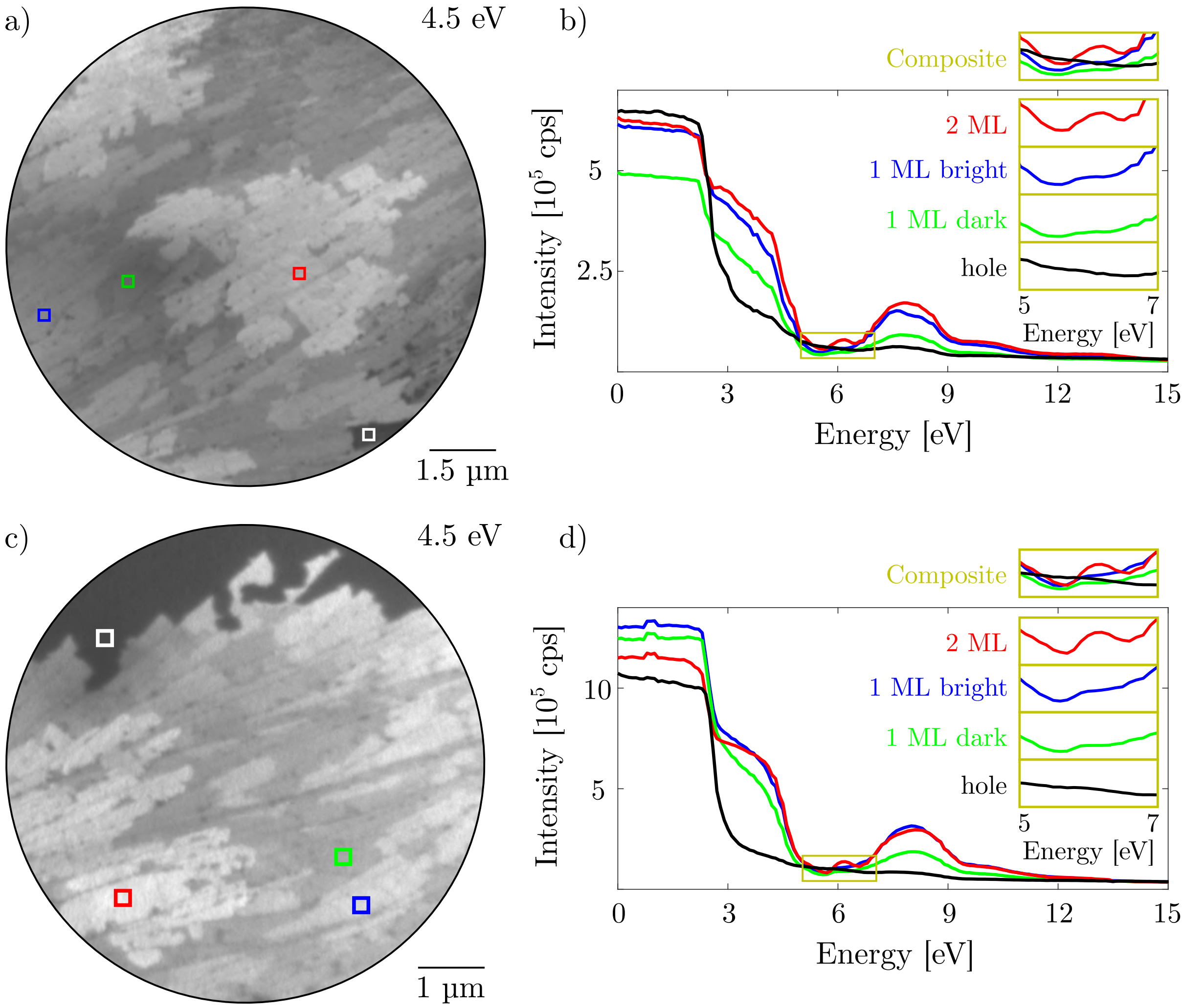

Figure 3.17: BF-IV analysis of two different regions belonging to (a) the center and (c) the edge of the pentacene island. The areas used for plotting the IV curves in (b) and (d) are highlighted by colored squares. The colors of the IV curves correspond to the colors of squares (except for the black curve, which comes from the white square for better visibility). The number of local minima in the highlighted energy interval 5–7 eV corresponds to the number of pentacene monolayers. Measured with an energy step of 0.1 eV.

In relation to the evaluation of IV curves, one feature of the instrument needs to be mentioned. Since the dependence starts at an electron energy of 0 eV, at this energy the initial intensity from all imaged regions should be the same. However, this is not true, because the detector is partially burned out from frequent and long PEEM measurements when a large number of electrons is detected. This is shown in Figure 3.18a (marked with an orange arrow). Since this burn out is not uniform, the IV curves from different regions do not start at the same intensity. Hence, for example, at an energy of approximately 8 eV the intensity from some brighter gray areas (blue square in Figure 3.18b, corresponding to Figure 3.17c above) will exceed that from the pentacene bilayer (red square in Figure 3.18b, corresponding to Figure 3.17c above). This effect must be considered for proper data interpretation.

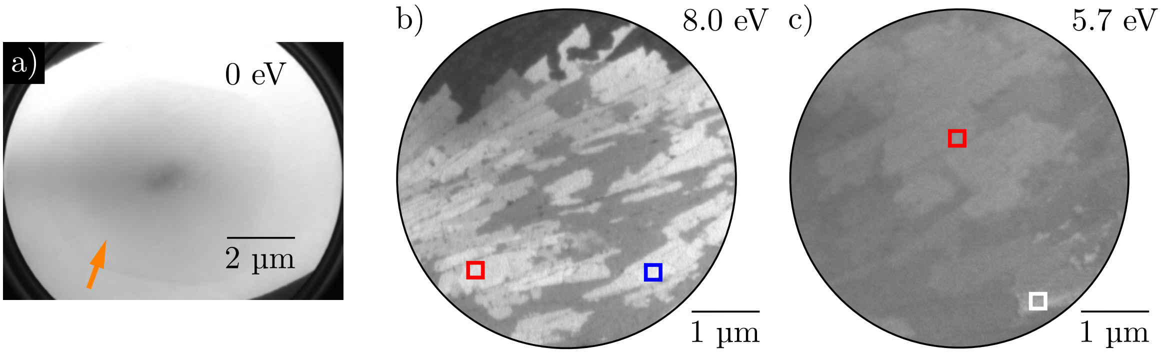

Figure 3.18: (a) BF image of the sample measured at 0 eV in the so-called mirror mode, where all electrons are reflected before reaching the surface. In the ideal case, the intensity should be the same over the entire surface region. However, the central part of the detector is burned out (marked with an orange arrow) due to the long-term measurements in PEEM mode. (b) BF image of the region from Figure 3.17c measured at 8 eV, where bright areas of the pentacene monolayer (blue square) appear brighter than the bilayer (red square). This is caused by the inhomogeneous burn out of the detector. (c) BF image of the region from Figure 3.17a measured at 5.7 eV where the hole in the pentacene island (white square) appears brighter than the pentacene bilayer (red square). This is because the pentacene bilayer has a local minimum of the reflected intensity at given energy. This phenomenon would be observed even in the case of an ideal detector, see Figure 3.19.

However, when the dependencies are normalized, the mutual contrast between individual regions is preserved over the entire range of most commonly used energies, i.e., 4–13 eV. Thus, over the entire range of these energies, the brightest areas correspond to the bilayer of molecules, followed by two distinct gray areas corresponding to the pentacene monolayer on top of the two rotational domains of the δ-BTB molecules, and the darkest regions correspond to the holes in the pentacene monolayer. The only exception occurs around 5.7 eV, where the regions corresponding to the holes in the pentacene islands appear even brighter than the regions of the bilayer of molecules (Figure 3.18c, corresponding normalized IV curves in Figure 3.19b).

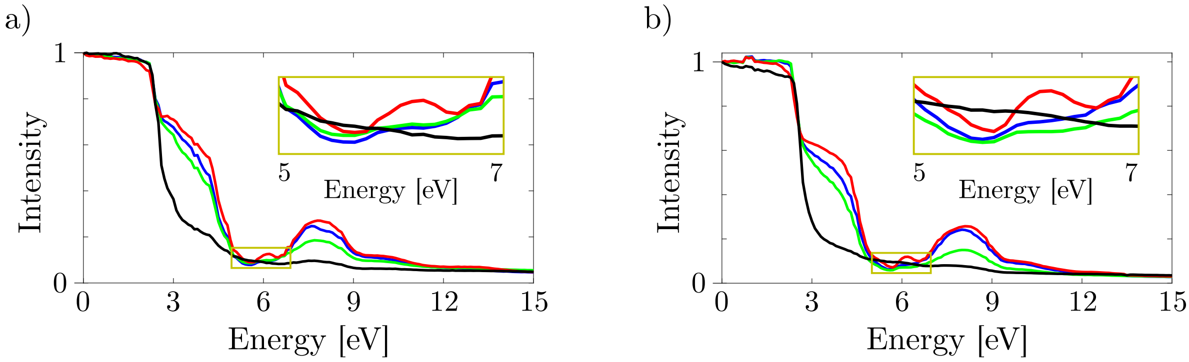

Figure 3.19: Normalized IV curves from (a) Figure 3.17b and (b) Figure 3.17d. At the most frequently used energies, i.e. 4–13 eV, the mutual contrast between the individual areas of the pentacene islands is preserved. The exception is a small interval of energies around 5.7 eV, where the holes in the pentacene islands appear brighter than the pentacene islands.

3.5.2. Electron beam damage

Another factor that affects the measured intensity is the so-called electron beam damage. The beam damage is significant when a long measurement of one region of the sample is made while using electrons of energy higher than 10 eV. In this case, the contrast between pentacene areas on top of the individual rotational domains of δ-BTB is reduced and the pentacene layer appears dark. This can be seen in Figure 3.20 measured in BF mode at 14.5 eV. The image has not been cropped to show the shape of the electron beam. At the bottom of Figure 3.20a can be seen that the area corresponding to the pentacene layer appears dark. This dark region was previously illuminated with 14.5 eV electrons for about a minute, after which the sample was moved to illuminate the interface between the previously measured and the newly measured region. As can be seen in Figure 3.20b, the newly illuminated area begins to darken after only fifteen seconds. It appears almost as dark as the area at the bottom of the image after 30 seconds (Figure 3.20c). This darkening under the electron beam is clearly visible in the case of the pentacene layer. A minor change can be also seen in the underlying δ-BTB layer after long irradiation times (>1 min). Therefore, it must be taken into account that the gradual decrease in intensities in the IV curves (Figure 3.17 and 3.19) at energies over 10 eV is partially due to electron beam damage.

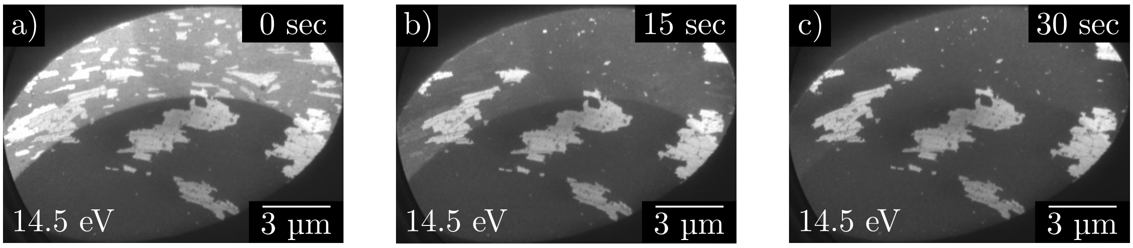

Figure 3.20: Uncropped BF images showing the darkening of the pentacene layer illuminated by electrons with energy 14.5 eV. The area that has been previously illuminated by the electron beam is at the bottom of the images, and at the top of the images is the newly illuminated area. As can be seen, after only thirty seconds the entire illuminated area corresponding to the pentacene layer is darkened because of the electron beam damage.

3.5.3. Dark field and microdiffraction analysis

The diffraction pattern of the pentacene layer consists of many distinct diffraction spots belonging to individual rotational domains of the pentacene molecules. Since we aim to determine the unit cell of pentacene molecules, for which it is convenient to separate the diffraction spots of the individual rotational domains, we had to measure the microdiffraction images. Before that, we measured DF images to see how large the regions of individual rotational domains were. We chose the most intense pentacene spots for DF analysis. The chosen spots are marked in Figure 3.21a. Since the δ-BTB molecules serving as a substrate have the 3-fold symmetry, we expected three different orientations of pentacene molecules for each underlying δ-BTB rotational domain and DF complementarity of the opposite spots (w.r.t. $(0, 0)$ spot).

Figures 3.21b and 3.21c show BF images of two different areas where DF images were measured. Figures 3.21e and 3.21f show the composition of individual DF images of these areas, while the colors of the domains in the DF compositions correspond to the colors of the marked diffraction spots in the diffraction pattern in Figure 3.21a. Diffraction spots belonging to the pentacene domains on top of the second rotational domain of underlying δ-BTB molecules are marked in Figure 3.21d.

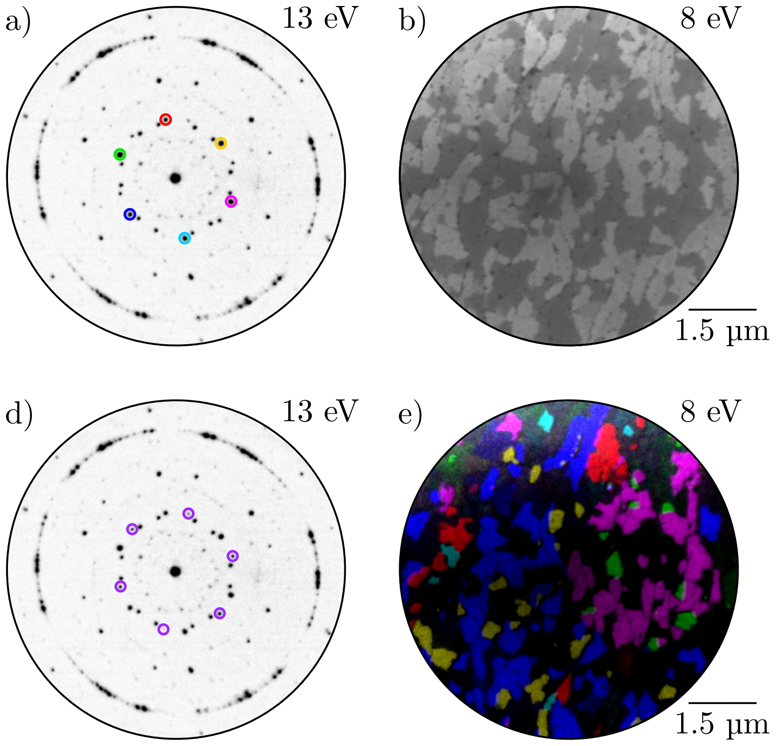

Figure 3.21: (a) Diffraction pattern of the pentacene layer. The diffraction spots from which we took DF images are marked in color. (b, c) BF images of the two areas from which we took DF images. (e, f) Composites of DF images corresponding to the given areas. Since the colors do not overlap, each diffraction spot corresponds to a different pentacene domain. Half of the surface in composites appears dark since we measured diffraction spots belonging to the pentacene domains on top of just one rotational domain of underlying δ-BTB molecules. (d) Diffraction pattern with marked spots which correspond to the pentacene layer on top of the second rotational domain of underlying δ-BTB molecules

Surprisingly, the regions contributing to the opposite diffraction spots are not identical. The possible explanation is that the top pentacene layer is shifted with respect to the substrate molecules in two directions.

As can be seen, colored areas in the DF composites correspond very precisely to the dark areas in the BF images, i.e., to only one rotational domain of the underlying δ-BTB molecules. This means that each of the rotational domains of δ-BTB can serve as a substrate for 6 non-identical pentacene domains.

Another important fact affecting the following measurements is that the regions of individual domains are often only a few hundred nm in diameter. We recognized the effect of this finding when measuring microdiffraction images, because even when using a fourth diffraction aperture with a diameter of 370 nm, most of the obtained microdiffraction images were a combination of diffraction spots corresponding to two or more different domains.

Even so, we managed to obtain 6 out of 12 microdiffraction patterns (Figure 3.22a), from which we can propose the unit cell. Their composite and comparison with the diffraction pattern corresponding to all 12 rotational domains of pentacene molecules can be seen in Figure 3.22c and Figure 3.22b.

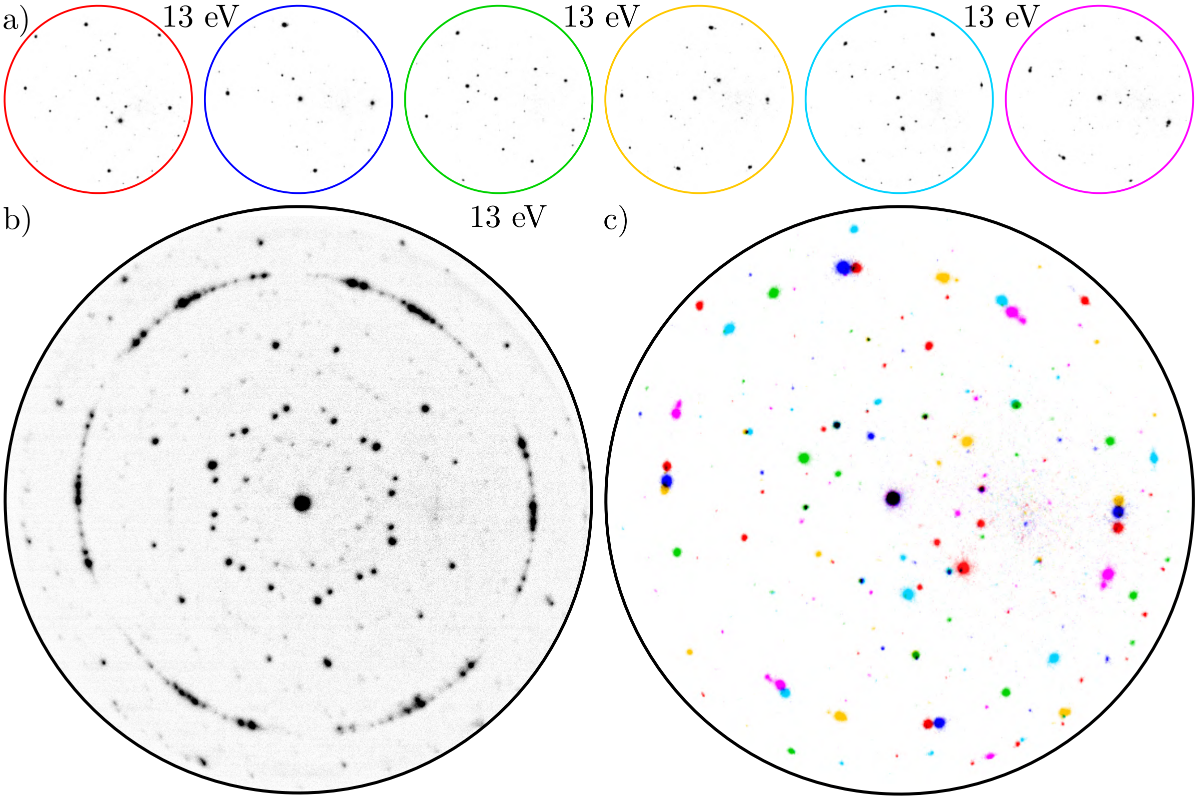

Figure 3.22: (a) Microdiffraction images belonging to six of the twelve rotational domains of pentacene molecules. Unfortunately, due to the small size of the islands corresponding to the individual rotational domains, we were unable to obtain all 12 microdiffraction patterns belonging to each of the pentacene domains. (b) Diffraction of a pentacene island compared to (c) the composite of 6 microdiffraction patterns of individual rotational domains.

3.5.4. Unit cell of pentacene molecules

The unit cell was proposed using ProLEED Studio software. This is a software developed primarily for the purposes of our research group, which is currently in the testing phase. Software and its details will be published in the future. The conversion from real to reciprocal space is described by the equations presented in Chapter 2.5.2, describing the theory of diffraction.

First, we describe the unit cell of δ-BTB layer on the Ag(111) substrate. Ag(111) has a hexagonal surface atom arrangement with real lattice vectors of length 0.288 nm that make an angle of 120 °. From diffraction patterns we found a perfect match for δ-BTB supercell within matrix notation

$$\begin{pmatrix} 5 & 1 \\ 1 & -4 \end{pmatrix}. \tag{3.1}$$

In our model (Figure 3.23a), the blue spheres represent silver atoms, the black spheres correspond to the corners of the unit cell δ-BTB periodicity, the black arrows represent unit vectors and the unit cell is in red. The unit vectors are 1.32 nm long and make an angle of 120 °. The corresponding diffraction model, including the reciprocal cell, can be seen in Figures 3.23b and 3.23c. As can be noticed, the diffraction spots are represented here by red and green spheres. Each color corresponds to one rotational domain, and their mutual rotation in reciprocal space is equal to 21.8 °. Figure 3.23d and Figure 3.23e are attached for comparison with experimental data.

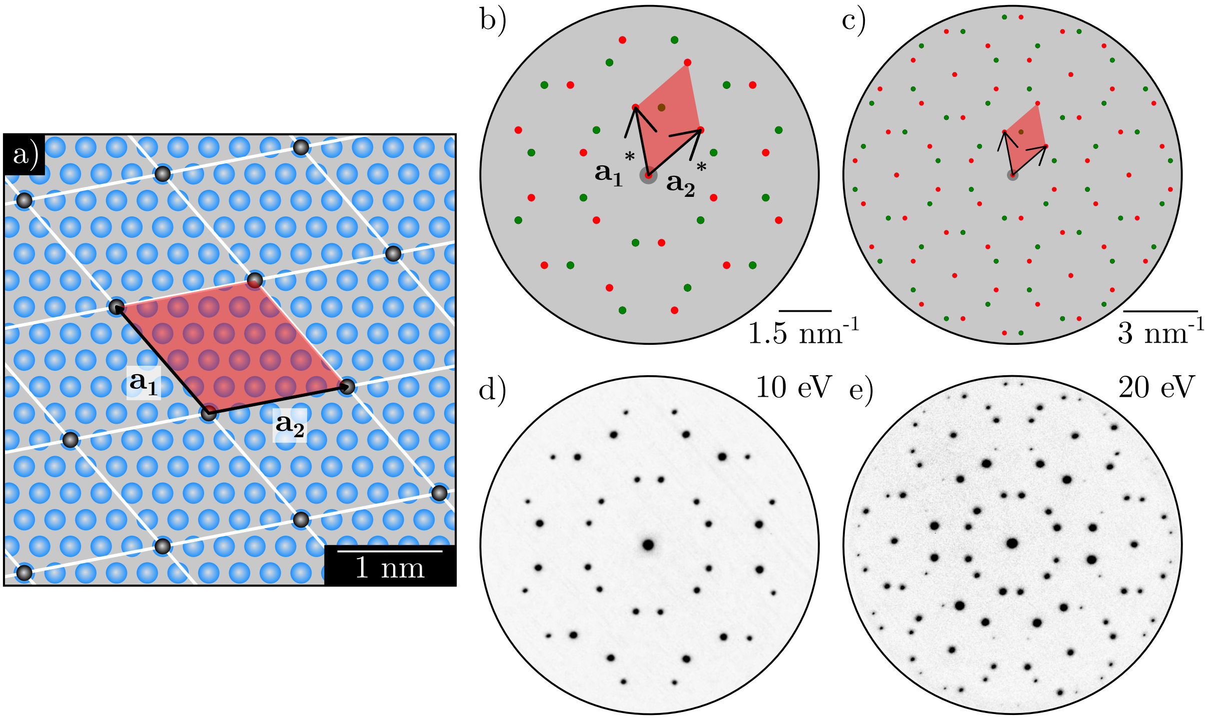

Figure 3.23: (a) The proposed unit cell of δ-BTB molecules. Blue spheres correspond to silver atoms, black spheres represent the δ-BTB periodicity, black arrows show unit vectors and the red area corresponds to the unit cell. (b, c) Diffraction model corresponding to the proposed δ-BTB unit cell. (d, e) Measured δ-BTB diffraction patterns.

We cannot accurately determine the rotation of molecules within the unit cell. For this purpose, density functional theory (DFT) calculations are required. These were performed by Dr. Jakub Planner and the results agreed with our proposed unit cell (Figure 3.24). Additionally, they provided information about the rotation of BTB molecules within the unit cell. As in our proposed unit cell (Figure 3.23), silver atoms of the substrate are represented by blue spheres. Carbon atoms of BTB molecules are in black, oxygens in red and hydrogens in light red. It can be noticed that all the carboxylic groups are deprotonated and interact with the silver substrate.

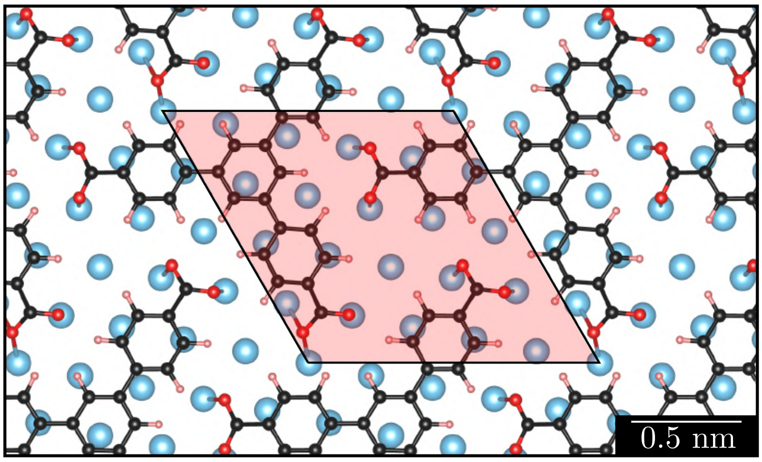

Figure 3.24: DFT simulation of the δ-BTB molecular arrangement. Silver atoms of the substrate are represented by blue spheres, carbon atoms of BTB molecules are in black, oxygen atoms in red and hydrogen atoms in light red. Performed by Dr. Jakub Planner.

This unit cell was subsequently used as a substrate for pentacene. Since the diffraction pattern corresponding to the pentacene layer is more complex than in the case of δ-BTB, we had to use microdiffraction images to create the unit cell. The best of them, with the reciprocal cell already marked, can be seen in Figure 3.25a. The proposed unit cell for pentacene molecules can be seen in Figure 3.25c and the corresponding diffraction model of one pentacene domain in Figure 3.25b. Black spheres correspond to the position of BTB molecules and red spheres to the position of pentacene molecules.

We propose that pentacene molecules have adapted to the superlattice of BTB molecules within matrix notation

$$\begin{pmatrix} -\frac{4}{9} & \frac{10}{9} \\ -\frac{5}{9} & \frac{1}{9} \end{pmatrix}. \tag{3.2}$$

The length of the unit vectors is $\mathbf{a}_1 = 0.805\,\mathrm{nm}$ and $\mathbf{a}_2 = 1.847\,\mathrm{nm}$, making an angle of approximately $34.9\,°$. In real space, the substrate lattice is marked in black and the pentacene lattice in red.

It can be noticed that not all experimentally obtained diffraction spots have their counterpart in the model, and conversely, not all diffraction spots corresponding to our proposed unit cell were experimentally measured. It is important to note that many of the weak diffraction spots obtained from the model will overlap with the background in real measurements. On the contrary, in the experimentally measured microdiffraction pattern, there are also diffraction spots corresponding to a higher-order periodicity, which could be precisely determined by combining the results from STM and DFT calculations.

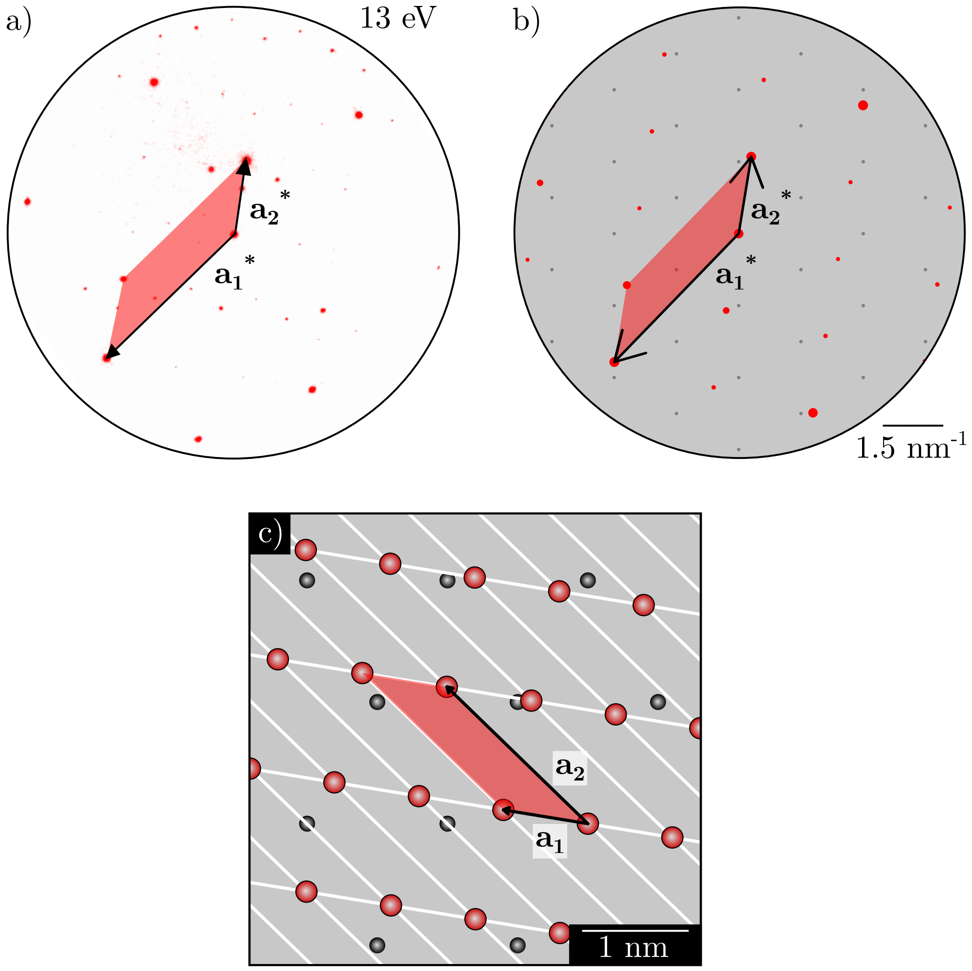

Figure 3.25: (a) Measured microdiffraction pattern. Primitive translation vectors of the reciprocal lattice are highlighted together with the reciprocal cell. (b) The diffraction model of the proposed unit cell of pentacene shown in (c). Black spheres correspond to the substrate (δ-BTB) periodicity, red spheres to the proposed pentacene periodicity, unit vectors and the unit cell are highlighted.

From the microdiffraction model of the one domain of pentacene molecules, we subsequently created a diffraction model of all pentacene domains and we compared it with the measured diffraction pattern (Figure 3.26). We achieved this by having knowledge of the domain rotations described in the previous chapter. First, we rotated the microdiffraction model by 180 ° to get the second domain, which probably belongs to the top layer offset. Next, we rotated both by 60 ° and 120 ° relative to the central spot to get all 6 observed domains belonging to the one rotational domain of the underlying δ-BTB molecules. Subsequently, the composition of these spots needs to be rotated by 21.8 ° to obtain the diffraction spots of pentacene domains on top of the second rotational domain of underlying δ-BTB molecules.

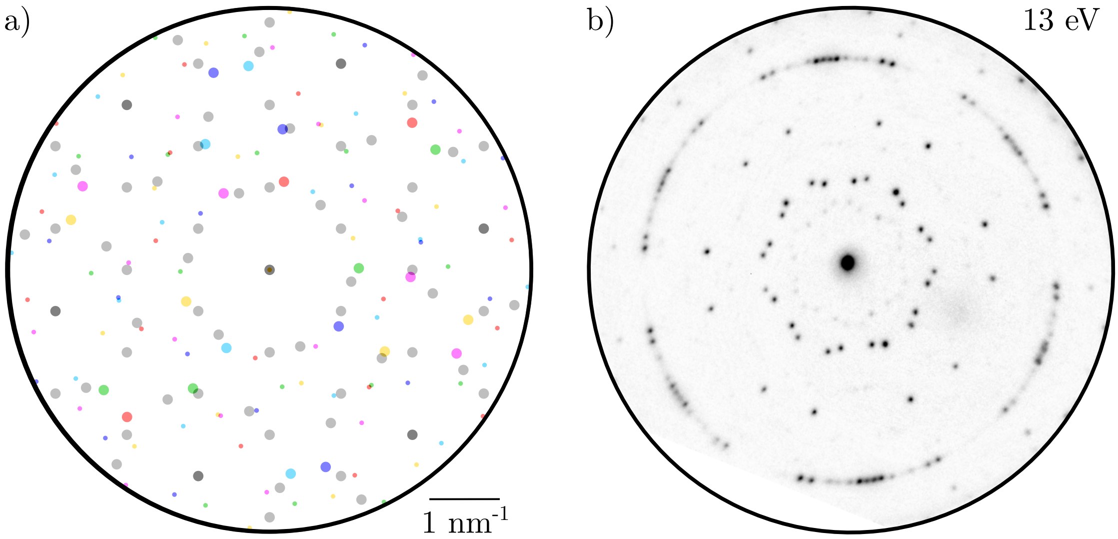

Figure 3.26: (a) Diffraction model corresponding to the proposed unit cell of all domains of pentacene molecules. (f) Measured diffraction pattern of the pentacene layer.

In contrast to our diffraction model (where opposite diffraction spots are represented by the same colors), opposite spots do not belong to the same domains in real measurements. The proof of this statement is also provided by the two microdiffraction patterns shown in Figure 3.27. As can be seen, they show the same diffraction spots, only the intensities of the circled diffraction spots are opposite. The possible explanation is that the top pentacene layer is shifted with respect to the substrate molecules in two directions.

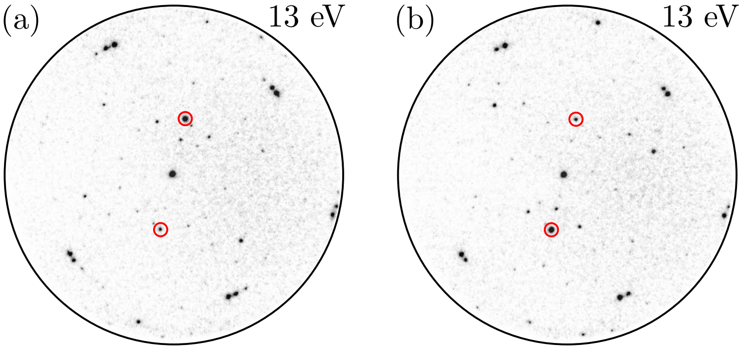

Figure 3.27: Two microdiffraction patterns. Diffraction spots that changed the intensity ratio after the measured area was changed (500 nm step) are marked in red. Based on these microdiffraction patterns and DF composites, we propose that each rotational domain of pentacene molecules has two different mutual displacements with respect to the underlying δ-BTB molecules.

3.5.5. STM measurements

Our proposed unit cell describes the periodical arrangement of pentacene molecules. To verify this model and also to determine the orientation of pentacene molecules within the unit cell, we decided to perform STM measurements. However, it was a complicated task for several reasons. First of all, pentacene grows on the surface in the form of large islands or dendritic structures, often several hundred µm apart. However, our STM does not allow macroscopic movement in the x and y axes. The measured area after the tip approaching is approximately 2 × 2 µm. If there is no pentacene island in the given area, it is necessary to withdraw completely with the tip and then mechanically move the sample.

Furthermore, there was a problem with the tip approach mechanism. After RT STM measurement was performed, the tip often crashed to the sample surface when the withdrawal was started. At temperatures below RT, this occurred at the beginning of each withdrawal. Therefore, every time the examined area was changed, it was necessary to prepare the atomically sharp tip again, which considerably lengthened the individual measurements.

Figure 3.28 shows the RT STM image of the surface at the beginning of the fourth growth stage of pentacene when needle-like structures started to appear. In the upper left corner, two BTB rotational domains, separated by an atomic step-edge, can be seen. The right half of the image is blurred. Due to the scanning direction (from top to bottom), we would expect smearing across the entire width of the image in the case of a blunt tip. However, in this case, the left part of the image is sharp, while the right part is blurred. Based on this, we assume that pentacene molecules are weakly bound to the surface, and scanning with the tip across the molecules causes them to move, which results in a blurred image. This would also be consistent with the height profile, which shows that the step height difference between the BTB molecules and the blurred region (approx. 0.25 nm) is smaller than the Ag(111) step-edge height difference (0.288 nm). This could correspond to the flat-lying pentacene molecules.

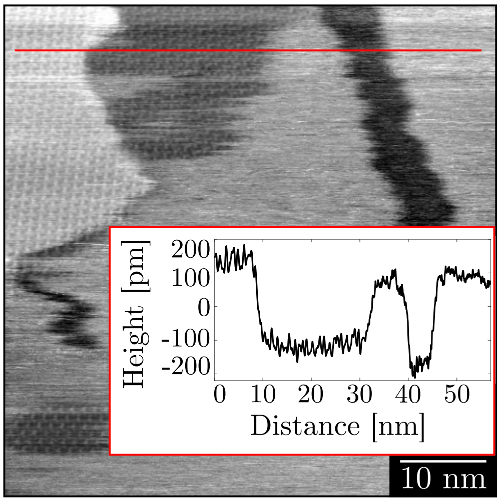

Figure 3.28: The RT STM image of the possible edge of the pentacene island. There are two rotational domains of underlying δ-BTB molecules in the upper left corner, the rest of the image is blurred. The step height difference between sharp and blurred areas is smaller than the Ag(111) step edge height difference, which could correspond to the flat-lying pentacene molecules. Measured at $U_S = 0.2$ V, I = 50 pA.

To minimize blurring, we also tried to measure the pentacene arrangement at lower temperatures. The STM in the CEITEC laboratories is not equipped with a cryostat and must be cooled externally using liquid nitrogen. Although we gradually optimized the cooling efficiency (with the help of Dr. Zdeněk Jakub), we were able to reach just 110 K. After the stage was unlocked for measurement purposes, the thermal contact between the stage and the cooled block became worse, so the temperature rose approx. by 5 °C per hour.

Figures 3.29a and 3.29b show region of disordered BTB molecules measured at 135 K. Since these regions of disordered BTB molecules were only captured at low temperatures, we cannot determine whether they are present on the surface at room temperature or not. A possible explanation could be that during the transformation of the molecules into δ-phase, decarboxylation of the molecules occurred at these regions, which caused their disorder. From the number of measured images, we estimate that these disordered areas cover less than 1 % of the surface and do not have a major influence on the work function or the growth of subsequent layers.

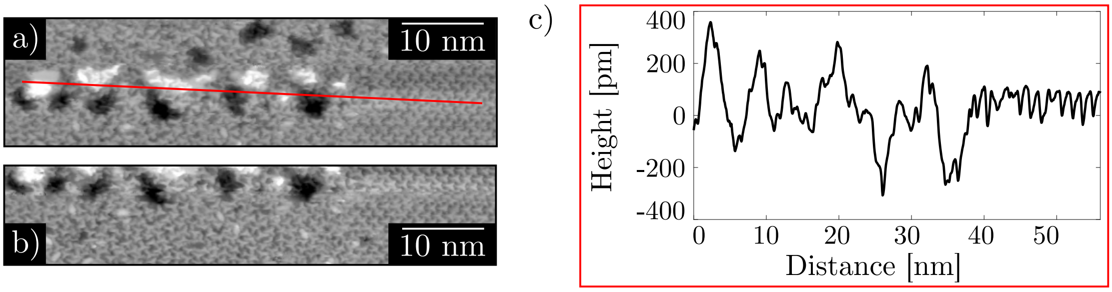

Figure 3.29: (a, b) STM images of the region of disordered BTB molecules (left part of the images). Due to the amount of images taken, we assume that these areas cover less than 1 % of the surface and do not fundamentally affect the work function and the growth of subsequent layers of pentacene. Measured at 135 K, $U_S = 1.0$ V, $I = 50$ pA. (c) Height profile of the region of disordered BTB molecules.

Unfortunately, due to the problems mentioned above, we were not able to measure the arrangement of pentacene molecules. Since the pentacene surface coverage was approximately 20 % in the form of large islands, the chance of approaching an area with a pentacene island was the same. If we could precisely move the tip in the x and y axes, or if we did not break the tip every time we tried to withdraw from the sample surface, it would be possible to measure the arrangement of the molecules. We took only a few images similar to Figure 3.30a. As can be seen, there are small clusters on the surface, often several layers high (Figure 3.30b). We were unable to distinguish whether it is pentacene or not. It is possible that some part of the molecular gas condensed in the form of these small clusters at lower temperatures. Considering the time spent in the UHV since deposition (less than 24 hours), it is unlikely that these are impurities from the surroundings. Similar coverage of these clusters was also measured 5 days after deposition. In the case of adsorbed contaminants, we would expect increasing coverage over time.

The height profile in Figure 3.30c shows that during the last measurements, there were step bunches on the surface. This was also noticed during measurements in PEEM and BF modes. In the last measurement, it significantly affected the growth of both the underlying δ-BTB layer and the subsequent pentacene layer, see the next chapter.

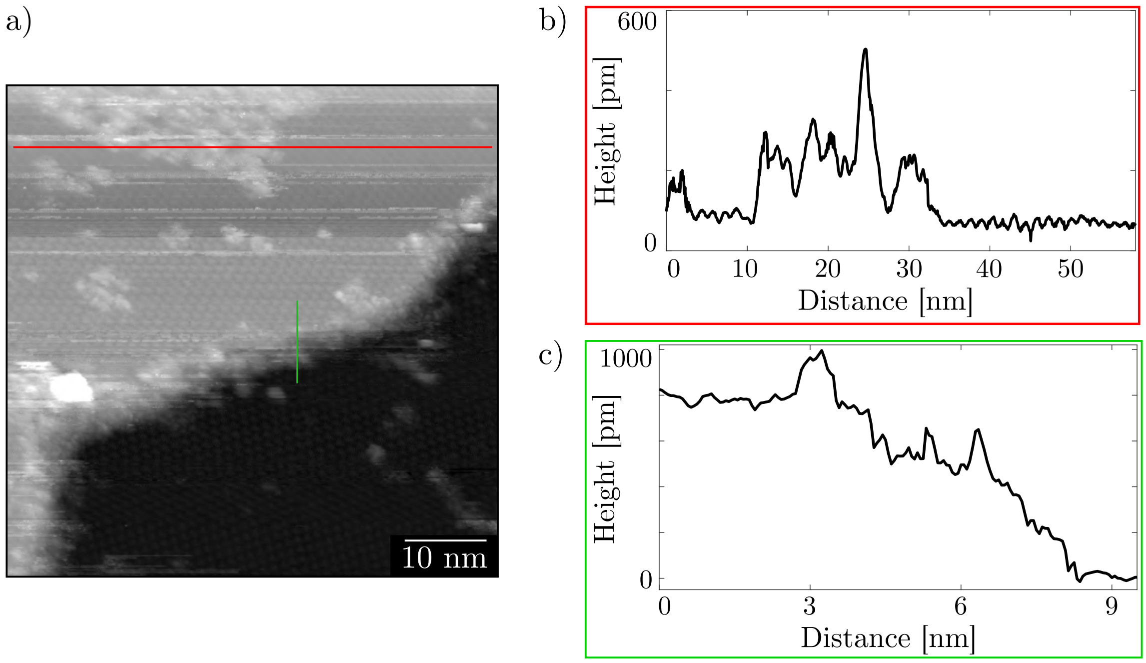

Figure 3.30: (a) STM image of the clusters that appeared on the surface after cooling to less than 135 K. We propose that these may be condensed pentacene molecules. Measured at 135 K, $U_S = 1.0$ V, $I = 50$ pA. (b) Height profile of one of the larger clusters. (c) Height profile of a step bunch that was formed on the crystal surface during the last experiments.

3.5.6. XPS and work function measurements

In this chapter, we first complement the previously presented XPS results and then analyze the UPS measurements to obtain information about the changes in the work function. Figure 3.5 has already provided information about the position of the carbon and oxygen peaks in XPS after the deposition of BTB molecules and their subsequent transformation to a well-ordered δ-phase. As shown in Figure 3.31, after 120 minutes of pentacene deposition (corresponding to the state before the second pentacene layer started to grow), there was a further shift of the carbon peak toward lower binding energies. The position of the O1s peak remained unchanged, as did the position of the Ag3d peak, which did not change throughout the experiment. After another 150 minutes of pentacene deposition (corresponding to the state when the needle-like structures began to grow), there was no further shift of the C1s peak.

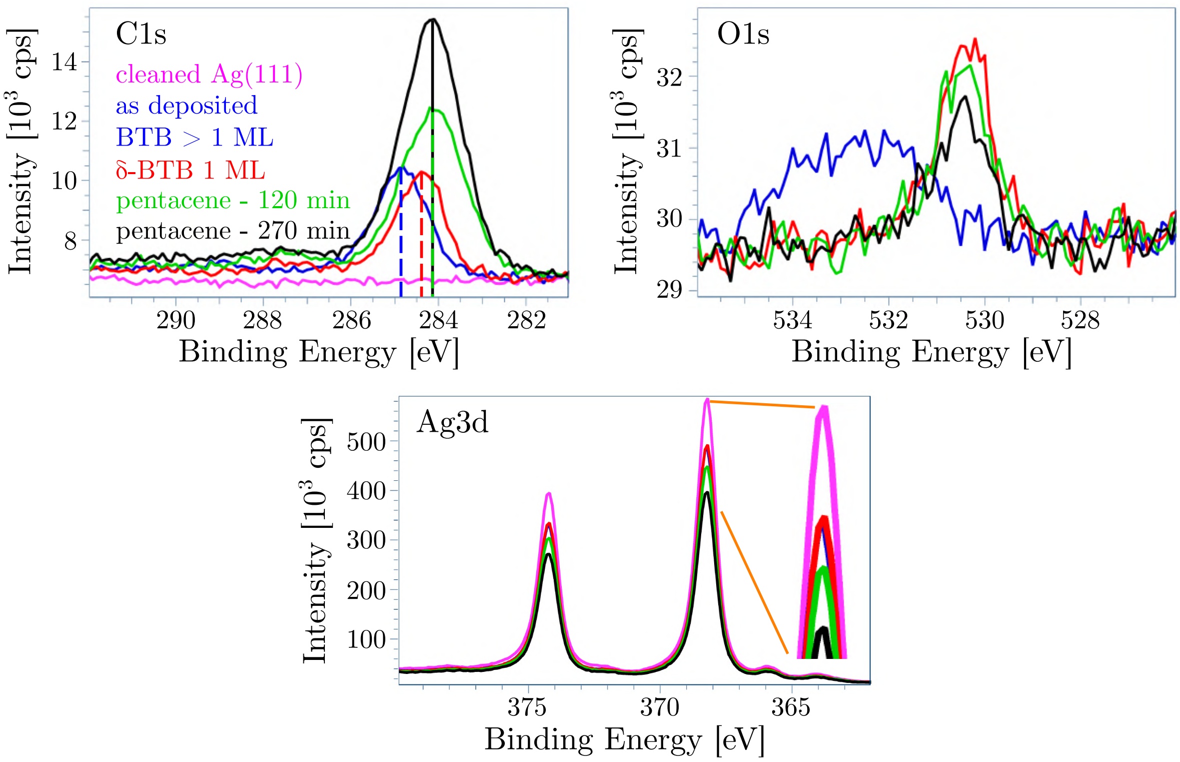

Figure 3.31: XPS spectra after each step of the system preparation. Deposition of the first pentacene layer caused the carbon peak to shift further towards lower binding energies. The subsequent pentacene deposition, during which mainly the islands of the second layer grew, did not result in a significant shift of the carbon peak. Measured in normal emission mode at RT with Mg X-ray source operating at power P = 300 W.

Before describing the UPS results, it is necessary to show the state of the sample during each measurement. In the beginning, the Ag(111) crystal was cleaned by several cycles of sputtering-annealing. Deposition of BTB molecules took place intentionally several tens of minutes longer than usual to ensure that at least 1 ML was deposited. The surface of the sample after the BTB deposition was checked in LEEM before the UPS measurement. As already stated in Chapter 3.2, it is difficult to distinguish whether the coverage of as-deposited BTB molecules is above 1 ML or below 1 ML using BF LEEM measurements. Due to the longer than usual deposition, we deduced from Figure 3.32a that the coverage is essentially higher than 1 ML, and at this stage, the UPS spectra (valence band, secondary electron cut-off position and Fermi-edge position) were measured. However, after transforming the molecules to the δ-phase, we found that the coverage was lower than 1 ML (Figure 3.32b). Retrospectively, we determined the coverage of molecules in the as-deposited phase to be approximately 70 % (holes in the BTB layer are dark areas marked with a red arrow). This should be taken into account when considering the effect of the as-deposited BTB layer on the change of work function.

Thus, more molecules were deposited and transformed so that the δ-phase surface coverage was 1 ML. The state of the surface before the UPS measurement can be seen in Figure 3.32c. This time the layer was not completely compact as in the previous measurements. This was most likely due to the existence of step bunches (Figure 3.30c). If there are only step-edges on the cleaned Ag(111) surface, coverage of BTB molecules could be achieved even near these step-edges. However, in the case of the existence of step bunches (according to Figure 3.30c up to three times as high as step-edges), the cover layer is probably not formed around these step bunches (marked with green arrows), which is later reflected in the pentacene growth. Still, the δ-BTB coverage is higher than 95 %.

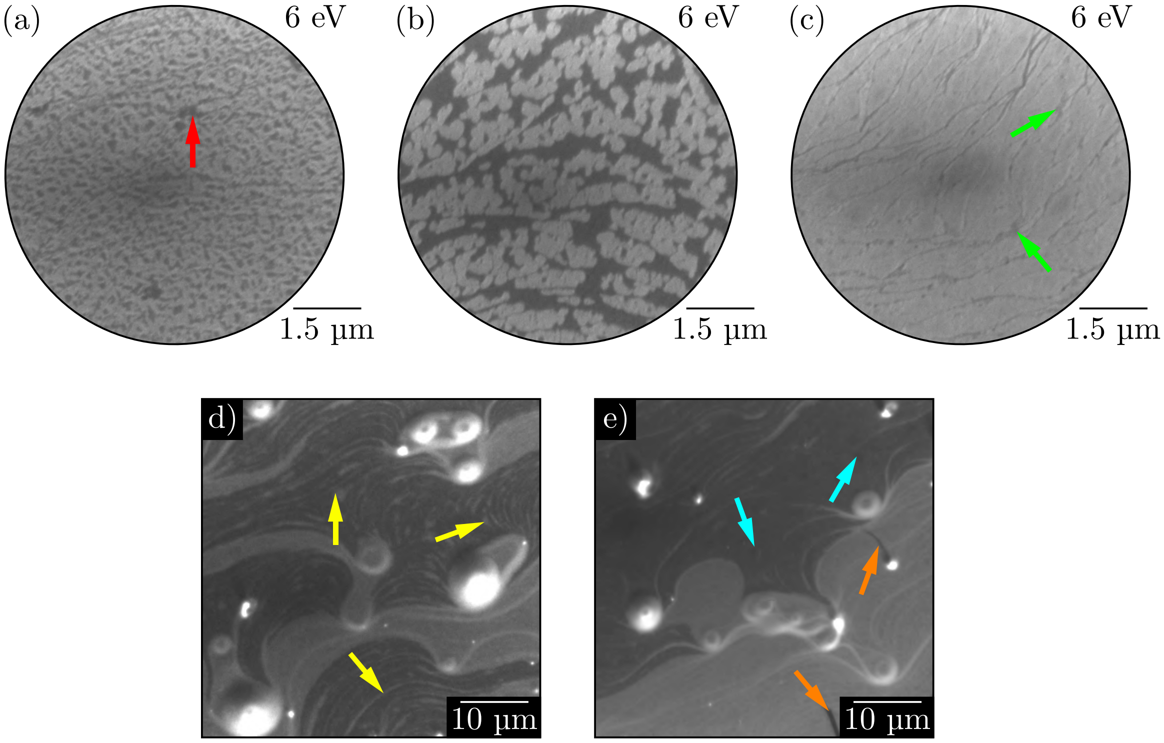

Figure 3.32: (a) BF image of the sample after the deposition of BTB molecules. Retrospectively, we determined that the dark areas were holes in the BTB layer (marked with a red arrow) and the coverage was approximately 70 %. (b) BF image of the sample after transforming the initial amount of BTB molecules to the δ-phase. (c) BF image of a monolayer of δ-BTB molecules. Due to numerous step bunches, an ideal homogeneous layer was not achieved. (d) PEEM image of the sample after 140 minutes of pentacene deposition. Pentacene islands are not as compact as usual (in this stage of the deposition, holes in the pentacene island are marked with yellow arrows), most likely because of the existence of step bunches and an imperfect δ-BTB layer. (e) PEEM image of the sample after 300 minutes of pentacene deposition. Gradually, most of the holes in the pentacene islands were filled and the islands of the second pentacene layer started to grow (marked with cyan arrows), and subsequently also the needle-like structures (marked with orange arrows).

Another UPS measurement was performed after 140 minutes of the pentacene deposition when the second layer islands began to grow on the most compact islands of the first pentacene layer. As can be seen from Figure 3.32d, the pentacene islands at this stage were not compact and no islands of the second layer were observed. Coverage of the first pentacene layer was determined as 15 – 20 %.

The last UPS measurement was performed after a total of 300 minutes of the pentacene deposition when the small islands of the second pentacene layer (marked with cyan arrows) were already visible even on the non-compact large islands of the first pentacene layer (Figure 3.32e). The same image shows the beginning of the growth of needle-like structures from the edges of the crystal defects (marked with orange arrows). Coverage of the first pentacene layer was determined as 20 – 25 %.

Individual UPS measurements can be seen in Figure 3.33. The Fermi-edge position for individual measurement was determined by the function for fitting this type of dependence in the SPECS Prodigy software. The secondary electron cut-off (SEC) position was determined by the intersection of two straight lines. The first was an extended linear fit of the steep part of the SEC peak. The second straight line was an extended linear fit of measured values before the onset of the SEC peak. We take the position of the intersection of these extended linear fits as the SEC position.

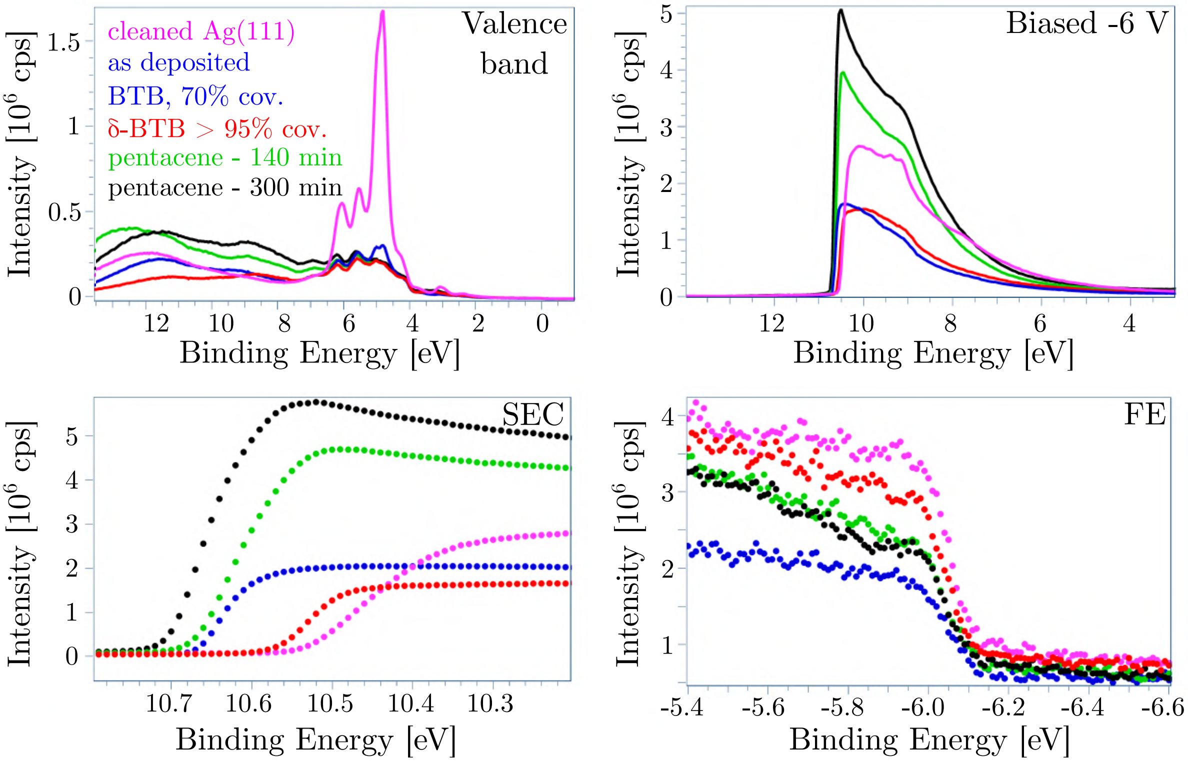

Figure 3.33: UPS spectra measured after each step of the system preparation. In the beginning, the valence band was measured, then the sample was biased to -6 V in order to be able to measure the onset of SEC. For a more accurate determination of the work function, SEC and Fermi-edge were measured with a smaller energy step. Measured at RT with He I (21.2 eV) source

The work function was subsequently determined from equation 2.12. The achieved results are summarized in Table 3.1.

Table 3.1: Work function in individual phases of the experiment.

Sample	**WF**
Cleaned Ag(111)	4.61 eV
Ag(111) + α-BTB 70 % coverage	4.48 eV
Ag(111) + δ-BTB > 95 % coverage	4.58 eV
Ag(111) + δ-BTB + pentacene 15 – 20 % coverage	4.47 eV
Ag(111) + δ-BTB + pentacene 20 – 25 % coverage	4.43 eV

3.5.7. Interpretation of changes of work function

The measured work function of 4.61 eV of cleaned Ag(111) is a bit higher in comparison to well-known values (approx. 4.53 eV). This deviation may be partially caused by numerous defects and step bunches on the surface and also by measurement inaccuracies. Adsorption of BTB molecules had the effect of reducing the work function to 4.48 eV, which was mainly caused by the push-back effect since the phenyl rings and protonated carboxylic groups of BTB molecules interact weakly with the substrate. The transformation of the molecules to the δ-phase caused an increase in the work function to 4.58 eV. The increase in work function was caused by the deprotonation of the carboxylic groups. There is a partial electron transfer of this newly created charge through the bonds between the carboxylate groups and the substrate.

Overall, the decrease and subsequent increase in the work function was much smaller than we have observed in (so far) unpublished measurements from the synchrotron. Here, a decrease in the work function after the adsorption of molecules of more than 0.4 eV was observed, and after the deprotonation of molecules the work function increased above the initial work function of the cleaned Ag(111). We are unable to determine exactly why our results for the BTB layer differ so much. The incomplete monolayer of as-deposited BTB molecules certainly plays a role in part. Therefore, these results still need to be verified.

Subsequent deposition of pentacene molecules again reduced the work function. After the first part of the deposition (140 minutes), the work function decreased to 4.47 eV. The estimated coverage at this growth stage was 15–20 %. Subsequent deposition (300 minutes in total) reduced the work function to 4.43 eV. Although the growth of the second layer of pentacene mainly occurred at this growth stage, there was also hole filling of existing islands and the growth of a few dendrites, increasing the coverage to 20–25 %. It was the increase in the coverage of the first layer that probably resulted in a further decrease in the work function. Unfortunately, we are not able to estimate the concentration of the molecular gas in the areas between the pentacene islands and the effect of the molecular gas on the change in work function. However, we can assume that a full layer of pentacene would reduce the work function much more, similar to the case of the direct deposition of pentacene on Ag(111) [6, 32].

There are several proposed mechanisms by which the pentacene deposition could reduce the work function of the sample. First of all, pentacene could have pushed the BTB molecules closer to the substrate by adsorption on the surface, which would partially push the electron cloud leaking from the bulk back. Another possible explanation is that the adsorption of pentacene molecules could have created a dipole between the δ-BTB layer and the pentacene layer that reduced the work function. Also, the adsorption of pentacene molecules may have caused the δ-BTB molecules to bend, creating an intrinsic dipole moment which affects the work function. Which of these phenomena occurred after the adsorption of pentacene molecules and contributed to the change in the work function has to be clarified by DFT calculations.

4. Conclusion

This thesis is focused on the growth and characterization of pentacene layers, one of the intensively studied organic semiconductors, on top of the Ag(111) crystal covered by a monolayer of carboxylic acid molecules. It has already been found that the first layer of pentacene deposited directly on this crystal surface does not form an organized structure [4, 5, 6]. Instead, it occurs on the surface as a two-dimensional (2D) highly mobile molecular gas. Therefore, we decided to first cover the surface of the silver crystal with a monolayer of well-ordered 4,4',4"-benzene-1,3,5-triyl-tribenzoic acid (BTB) molecules. This cover layer was supposed to positively influence the growth of subsequent layers of pentacene and ideally also change the work function of the substrate.

After silver substrate cleaning by several sputtering-annealing cycles under ultra-high vacuum (UHV) conditions, we proceeded to the deposition of BTB molecules. Our goal was to achieve a well-defined arrangement of molecules over the entire surface. However, it turned out to be very difficult to determine a full layer coverage of as-deposited BTB molecules using a low-energy electron microscope (LEEM). Moreover, the diffraction pattern corresponding to the as-deposited molecules was blurred, which indicated a not ideal arrangement of the molecules. However, these problems disappeared when the system was annealed. As a result, the molecules deprotonated and rearranged into a compact, well-defined structure, the coverage of which was possible to precisely determine by LEEM. This molecular arrangement was measured by scanning tunneling microscope (STM) and its chemical homogeneity was confirmed by X-ray photoelectron spectroscope (XPS). For these reasons, we used deprotonated BTB molecules in the so-called δ-phase arrangement as a cover layer for pentacene growth.

This cover layer influenced the pentacene growth and we divided this growth into four stages. Although the molecules appeared on the surface in the form of a 2D molecular gas at the beginning of the deposition, after a certain time, molecularly huge, often more than 0.2 mm wide, islands rapidly nucleated in the first growth stage. Subsequently, dendritic structures began to grow from these islands, and later islands of the second pentacene layer also grew on the compact islands of the first layer. However, after a few hours of deposition, needle-like structures began to grow on the still unfilled surface. Once the needle-like structures appeared, there was no longer expansion of the islands of the first pentacene layer. It was not possible to get rid of the needle-like structures by annealing without desorption of the pentacene islands at the same time. Since mainly the first layer has a fundamental influence on the change of work function of the system, we decided to always stop the deposition when needle-like structures appeared. The resulting coverage of the pentacene islands was $20-25\,\%$, depending on the particular experiment.

Subsequently, we characterized the grown pentacene layers. IV curves were measured to support our contrast interpretation of images taken by LEEM (Figure 3.17). Furthermore, we measured dark field images (Figure 3.21) and microdiffraction images (Figure 3.22), based on which we proposed a unit cell of pentacene molecules (Figure 3.25).

Unfortunately, we were not able to measure STM images of the pentacene arrangement. It turned out that pentacene molecules are weakly bound to the surface at room temperature, and scanning with the tip causes the molecules to move. A failure in the STM tip approach mechanism became apparent at low temperatures, due to which the tip always crashed into the surface when trying to withdraw. Together with the impossibility of moving in the x and y axes, these were difficult conditions to measure the pentacene arrangement.

In addition, the work function of the system was measured after individual steps of the preparation process (Table 3.1) using an ultraviolet photoelectron spectroscope (UPS). It turned out that the deposition of BTB molecules decreased the work function of the substrate due to the push-back effect. The subsequent transformation of the molecules, induced by the deprotonation of carboxylic groups, into the δ-phase caused an increase of the work function. Finally, pentacene deposition again reduced the work function. The decrease of the work function was not as significant as in the previous studies dealing with the pentacene growth on a pure Ag(111) [6, 32], which could be due to the low coverage of the surface with pentacene islands.

Overall, this thesis is the first step in the investigation of heterogeneous multilayers and the use of carboxylic acid molecules as cover layers for the growth of organic semiconductors. In the near future, we would like to describe the BTB cover layer and also its mixed phases with pentacene in more detail. Only such a comprehensive approach will enable a detailed description of the growth and properties of organic semiconductors.

Bibliography

[1] WALDRIP, M., JURCHESCU, O. D., GUNDLACH, D. J., et al. Contact Resistance in Organic Field-Effect Transistors: Conquering the Barrier. *Advanced Functional Materials*, 2020, **30**(20), 1904576. DOI: 10.1002/adfm.201904576. ISSN 1616-3028.

[2] BOUJU, X., MATTIOLI, C., FRANC, G., et al. Bicomponent Supramolecular Architectures at the Vacuum–Solid Interface. *Chemical Reviews*, 2017, **117**(3), 1407−1444. DOI: 10.1021/acs.chemrev.6b00389. ISSN 0009-2665.

[3] GOIRI, E., BORGHETTI, P., EL-SAYED, A., et al. Multi-Component Organic Layers on Metal Substrates. *Advanced Materials*, 2016, **28**(7), 1340−1368. DOI: 10.1002/adma.201503570. ISSN 1521-4095.

[4] DOUGHERTY, D. B., JIN, W., CULLEN, W. G., et al. Variable Temperature Scanning Tunneling Microscopy of Pentacene Monolayer and Bilayer Phases on Ag(111). *The Journal of Physical Chemistry C*, 2008, **112**(51), 20334−20339. DOI: 10.1021/jp804682v.ISSN 1932-7447.

[5] DUHM, S., BÜRKER, C., NIEDERHAUSEN, J., et al. Pentacene on Ag(111): Correlation of Bonding Distance with Intermolecular Interaction and Order. *ACS Applied Materials and Interfaces*, 2013, **5**(19), 9377−9381. DOI: 10.1021/am402778u. ISSN 1944-8244.

[6] LU, M.-C., WANG, R.-B., YANG, A., et al. Pentacene on Au(1 1 1), Ag(1 1 1) and Cu(1 1 1): From physisorption to chemisorption. *Journal of Physics: Condensed Matter*, 2016, **28**(9), 094005. DOI: 10.1088/0953-8984/28/9/094005. ISSN 0953-8984.

[7] OURA, K., KATAYAMA, M., ZOTOV, A. et al. *Surface Science*. First edition. Berlin; Heidelberg: Springer, 2003, xii, p. 440. ISBN 978-3-540-00545-2.

[8] LÜTH, H. *Solid Surfaces, Interfaces and Thin Films*. Fifth edition. Berlin; Heidelberg: Springer, 2010, xvi, p. 589. ISBN 978-3-642-13592-7.

[9] IBACH, H. *Physics of Surfaces and Interfaces*. First edition. Berlin; Heidelberg: Springer, 2006, xii, p. 646. ISBN 978-3-540-34709-5.

[10] MALI, K. S. and DE FEYTER, S. Principles of molecular assemblies leading to molecular nanostructures. *Philosophical Transactions of the Royal Society A: Mathematical, Physical and Engineering Sciences*, 2013, **371**(2000), 20120304. DOI: 10.1098/rsta.2012.0304.

[11] KÜHNLE, A. Self-assembly of organic molecules at metal surfaces. *Current Opinion in Colloid and Interface Science*, 2009, **14**(2), 157−168. DOI: 10.1016/j.cocis.2008.01.001. ISSN 1359-0294.

[12] MACLEOD, J. Design and construction of on-surface molecular nanoarchitectures: Lessons and trends from trimesic acid and other small carboxlyated building blocks. *Journal of Physics D: Applied Physics*, 2019, **53**(4), 043002. DOI: 10.1088/1361-6463/ab4c4d. ISSN 0022-3727.

[13] SCARBATH-EVERS, L. K., HAMMER, R., GOLZE, D., et al. From flat to tilted: Gradual interfaces in organic thin film growth. *Nanoscale*, 2020, **12**(6), 3834–3845. DOI: 10.1039/C9NR06592J. ISSN 2040-3372.

[14] LEE, W. H., PARK, J., SIM, S. H., et al. Surface-Directed Molecular Assembly of Pentacene on Monolayer Graphene for High-Performance Organic Transistors. *Journal of the American Chemical Society*, 2011, **133**(12), 4447–4454. DOI: 10.1021/ja1097463. ISSN 0002-7863.

[15] BRAUN, S., SALANECK, W. R. AND FAHLMAN, M. Energy-Level Alignment at Organic/Metal and Organic/Organic Interfaces. *Advanced Materials*, 2009, **21**(14-15), 1450–1472. DOI: 10.1002/adma.200802893. ISSN 1521-4095.

[16] FAHLMAN, M., FABIANO, S., GUESKINE, V., et al. Interfaces in organic electronics. *Nature Reviews Materials*, 2019, **4**(10), 627–650. DOI: 10.1038/s41578-019-0127-y. ISSN 2058-8437.

[17] MALLIARAS, G. and FRIEND, R. An Organic Electronics Primer. *Physics Today*, 2005, **58**(5), 53–58. DOI: 10.1063/1.1995748. ISSN 0031-9228.

[18] STARÁ, V., PROCHÁZKA, P., PLANER, J., et al. Tunable Energy-Level Alignment in Multilayers of Carboxylic Acids on Silver. *Physical Review Applied*, 2022, **18**(4), 044048. DOI: 10.1103/PhysRevApplied.18.044048

[19] PROCHÁZKA, P., GOSALVEZ, M. A., KORMOŠ, L., et al. Multiscale Analysis of Phase Transformations in Self-Assembled Layers of 4,4´-Biphenyl Dicarboxylic Acid on the Ag(001) Surface. *ACS Nano*, 2020, **14**(6), 7269–7279. DOI: 10.1021/acsnano.0c02491. ISSN 1936-0851.

[20] MRHÁČOVÁ, P. *Metal-organic interface for effective charge transfer.* [Bachelor thesis] Brno: Brno University of Technology. Faculty of Mechanical Engineering, 2022. Supervised by Ing. Pavel Procházka, Ph.D.

[21] PROCHÁZKA, P., KORMOŠ, L., SHAHSAVAR, A., et al. Phase transformations in a complete monolayer of 4,4´-biphenyl-dicarboxylic acid on Ag(001). *Applied Surface Science*, 2021, **547**, 149115. DOI: 10.1016/j.apsusc.2021.149115. ISSN 0169-4332.

[22] BARTELS, L. Tailoring molecular layers at metal surfaces. *Nature Chemistry*, 2010, **2**(2), 87–95. DOI: 10.1038/nchem.517. ISSN 1755-4349.

[23] RUBEN, M., PAYER, D., LANDA, A., et al. 2D supramolecular assemblies of benzene-1,3,5-triyl-tribenzoic acid: Temperature-induced phase transformations and hierarchical organization with macrocyclic molecules. *Journal of the American Chemical Society*, 2006, **128**(49), 15644–15651. DOI: 10.1021/ja063601k. ISSN 0002-7863.

[24] BANERJEE, K., KUMAR, A., CANOVA, F. F., et al. Flexible Self-Assembled Molecular Templates on Graphene. *The Journal of Physical Chemistry C*, 2016, **120**(16), 8772–8780. DOI: 10.1021/acs.jpcc.6b01638. ISSN 1932-7447.

[25] GUTZLER, R., SIRTL, T., DIENSTMAIER, J. F., et al. Reversible Phase Transitions in Self-Assembled Monolayers at the Liquid–Solid Interface: Temperature-Controlled Opening and Closing of Nanopores. *Journal of the American Chemical Society*, 2010, **132**(14), 5084−5090. DOI: 10.1021/ja908919r. ISSN 0002-7863.

[26] VELPULA, G., MARTIN, C., DAELEMANS, B., et al. "Concentration-in-Control" self-assembly concept at the liquid–solid interface challenged. *Chemical Science*, 2021, **12**(39), 13167−13176. DOI: 10.1039/D1SC02950A.

[27] LEE, S.-L., FANG, Y., VELPULA, G., et al. Reversible Local and Global Switching in Multicomponent Supramolecular Networks: Controlled Guest Release and Capture at the Solution/Solid Interface. *ACS Nano*, 2015, **9**(12), 11608−11617. DOI: 10.1021/acsnano.5b06081. ISSN 1936-0851.

[28] ZHANG, Y. and CAI, Y. L. The growth mechanism of graphene based on self-assembly of 1,3,5-Benzenetribenzoic acid on Ru(0001). *Surface Science*, 2021, **704**, 121746. DOI: 10.1016/j.susc.2020.121746. ISSN 0039-6028.

[29] KANG, J. H. and ZHU, X.-Y. Layer-by-Layer Growth of Incommensurate, Polycrystalline, Lying-Down Pentacene Thin Films on Au(111). *Chemistry of Materials*, 2006, **18**(5), 1318−1323. DOI: 10.1021/cm051990w ISSN 0897-4756.

[30] SCHROEDER, P. G., FRANCE, C. B., PARK, J. B., et al. Energy level alignment and two-dimensional structure of pentacene on Au(111) surfaces. *Journal of Applied Physics*, 2002, **91**(5), 3010−3014. DOI: 10.1063/1.1445286. ISSN 0021-8979.

[31] SMERDON, J. A. et al. Monolayer and bilayer pentacene on Cu(111). *Physical Review B*, 2011, **84**(16), 165436. DOI: 10.1103/PhysRevB.84.165436.

[32] JAECKEL, B., SAMBUR, J. B. and PARKINSON, B. A. The influence of metal work function on the barrier heights of metal/pentacene junctions. *Journal of Applied Physics*, 2008, **103**(6), 063719. DOI: 10.1063/1.2890415. ISSN 0021-8979.

[33] FRANCO-CAÑELLAS, A., DUHM, S., GERLACH, A., et al. Binding and electronic level alignment of π-conjugated systems on metals. *Reports on Progress in Physics*, 2020, **83**(6), 066501. DOI: 10.1088/1361-6633/ab7a42. ISSN 0034-4885.

[34] JOBST, J. et al. Nanoscale measurements of unoccupied band dispersion in few-layer graphene. *Nature Communications*, 2015, **6**(1), 8926. DOI: 10.1038/ncomms9926 ISSN 2041-1723.

5. List of used abbreviations

2D	Two-dimensional
7A, 8A, 9A	Heptanoic acid, octanoic acid, nonanoic acid
α-6T	α-Sexithiophene
BDA	4,4'-biphenyl dicarboxylic acid
BF	Bright field
BF-IV	Bright field intensity-voltage
BTB	4,4',4"-benzene-1,3,5-triyl-tribenzoic acid
CIL	Charge-injection layer
CoPC	Cobalt phtalocyanine
DF	Dark field
EA	Electron affinity
E_F	Fermi energy
ELA	Energy level alignment
HOMO(-c)	Highest occupied molecular orbital (-critical)
ICT	Integer charge transfer
IE	Ionization energy
LEED	Low-energy electron diffraction
LEEM	Low-energy electron microscopy
LTS	Linear transfer system
LUMO(-c)	Lowest unoccupied molecular orbital (-critical)
MBE	Molecular beam epitaxy
ML	Monolayer
OFETs	Organic field-effect transistors
OLED	Organic light-emitting diode
OPV	Organic photovoltaic
OS	Organic semiconductor
PEEM	Photoemission electron microscopy

PMMA	Polymethylmethacrylate
RT	Room temperature
STM	Scanning tunneling microscopy
TMA	Benzene-1,3,5-tricarboxylic acid
UHV	Ultra-high vacuum
UPS	Ultraviolet photoelectron spectroscopy
UV	Ultraviolet
vdW	Van der Waals
VL	Vacuum level
WF	Work function
XPS	X-ray photoelectron spectroscopy